TVD and ENO Applications to Supersonic Flows in 3D – Part I

EDISSON SÁVIO DE GÓES MACIEL
IEA – Aeronautical Engineering Division
ITA – Aeronautical Technological Institute
Praça Mal. do Ar Eduardo Gomes, 50 – Vila das Acácias – São José dos Campos – SP – 12228-900
BRAZIL
edisavio@edissonsavio.eng.br , http://www.edissonsavio.eng.br

Abstract: - In this work, first part of this study, the high resolution numerical schemes of Lax and Wendroff, of Yee, Warming and Harten, of Yee, and of Harten and Osher are applied to the solution of the Euler and Navier-Stokes equations in three-dimensions. With the exception of the Lax and Wendroff and of the Yee schemes, which are symmetrical ones, all others are flux difference splitting algorithms. All schemes are second order accurate in space and first order accurate in time. The Euler and Navier-Stokes equations, written in a conservative and integral form, are solved, according to a finite volume and structured formulations. A spatially variable time step procedure is employed aiming to accelerate the convergence of the numerical schemes to the steady state condition. It has proved excellent gains in terms of convergence acceleration as reported by Maciel. The physical problems of the supersonic flows along a compression corner and along a ramp are solved, in the inviscid case. For the viscous case, the transonic flow along a convergent-divergent nozzle is solved. In the inviscid case, an implicit formulation is employed to marching in time, whereas in the viscous case, a time splitting approach is used. The results have demonstrated that the Harten and Osher algorithm, in its ENO version, presents the best solutions in the inviscid compression corner and ramp problems; whereas the Lax and Wendroff algorithm has presented the best solution to the nozzle problem.

Key-Words: - Lax and Wendroff algorithm; Yee, Warming and Harten algorithm; Yee algorithm; Harten and Osher algorithm; TVD and ENO flux splitting, Euler and Navier-Stokes equations, Finite volume, Three-dimensions.

1 Introduction

Conventional shock capturing schemes for the solution of nonlinear hyperbolic conservation laws is linear and L_2-stable (stable in the L_2-norm) when considered in the constant coefficient case ([1]). There are three major difficulties in using such schemes to compute discontinuous solutions of a nonlinear system, such as the compressible Euler equations:

(i) Schemes that are second (or higher) order accurate may produce oscillations wherever the solution is not smooth;

(ii) Nonlinear instabilities may develop in spite of the L_2-stability in the constant coefficient case;

(iii) The scheme may select a nonphysical solution.

It is well known that monotone conservative difference schemes always converge and that their limit is the physical weak solution satisfying an entropy inequality. Thus monotone schemes are guaranteed not to have difficulties (ii) and (iii). However, monotone schemes are only first order accurate. Consequently, they produce rather crude approximations whenever the solution varies strongly in space or time.

When using a second (or higher) order accurate scheme, some of these difficulties can be overcome by adding a hefty amount of numerical dissipation to the scheme. Unfortunately, this process brings about an irretrievable loss of information that exhibits itself in degraded accuracy and smeared discontinuities. Thus, a typical complaint about conventional schemes which are developed under the guidelines of linear theory is that they are not robust and/or not accurate enough.

To overcome the difficulties, a new class of schemes was considered that is more appropriate for the computation of weak solutions (i.e., solutions with shocks and contact discontinuities) of nonlinear hyperbolic conservation laws. These schemes are required (a) to be total variation diminishing in the nonlinear scalar case and the constant coefficient system case ([2-3]) and (b) to be consistent with the conservation law and an entropy inequality ([4-5]). The first property guarantees that the scheme does not generate spurious oscillations. Schemes with this property are referred in the literature as total variation diminishing (TVD) schemes (or total variation non-increasing, TVNI, [3]). The latter property guarantees that the weak solutions are physical ones. Schemes in this class are guaranteed to avoid difficulties (i)-(iii) mentioned above.

[6] has proposed a very enlightening generalized formulation of TVD [7] schemes. Roe's result, in turn, is a generalization of [8] work. [9] incorporated the results of [6; 8] with minor modification to a one parameter family of explicit and implicit TVD schemes ([10-11]) so that a wider group of limiters could be represented in a general but rather simple form which is at the same time suitable for steady-state applications. The final scheme could be interpreted as a three-point, spatially central difference explicit or implicit scheme which has a whole variety of more rational numerical dissipation terms than the classical way of handling shock-capturing algorithms.

[12] applied a new implicit unconditionally stable high resolution TVD scheme to steady state calculations. It was a member of a one-parameter family of explicit and implicit second order accurate schemes developed by [3] for the computation of weak solutions of one-dimensional hyperbolic conservation laws. The scheme was guaranteed not to generate spurious oscillations for a nonlinear scalar equation and a constant coefficient system. Numerical experiments have shown that the scheme not only had a fairly rapid convergence rate, but also generated a highly resolved approximation to the steady state solution. A detailed implementation of the implicit scheme for the one- and two-dimensional compressible inviscid equations of gas dynamics was presented. Some numerical experiments of one- and two-dimensional fluid flows containing shocks demonstrated the efficiency and accuracy of the new scheme.

Recently, a new class of uniformly high order accurate essentially non-oscillatory (ENO) schemes has been developed by [13] and [14-16]. They presented a hierarchy of uniformly high order accurate schemes that generalize [17]'s scheme, its second order accurate MUSCL ("Monotone Upstream-centered Schemes for Conservation Laws") extension ([18-19]), and the total variation diminishing schemes ([3; 20]) to arbitrary order of accuracy. In contrast to the earlier second order TVD schemes which drop to first order accuracy at local extrema and maintain second order accuracy in smooth regions, the new ENO schemes are uniformly high order accurate throughout, even at critical points. The ENO schemes use a reconstruction algorithm that is derived from a new interpolation technique that when applied to piecewise smooth data gives high order accuracy whenever the function is smooth but avoids a Gibbs phenomenon at discontinuities. An adaptive stencil of grid points is used; therefore, the resulting schemes are highly nonlinear even in the scalar case.

In contrast to the earlier second order TVD schemes, which drop to first order accuracy at local extreme and maintain second order accuracy in smooth regions, the new ENO schemes are uniformly high order accurate throughout even at critical points. Theoretical results for the scalar conservation law and for the Euler equations of gas dynamics have been reported with highly accurate results. Preliminary results for two-dimensional problems were reported in [21].

[22] gives a very extensive survey of the state of the art of second order high resolution schemes for the Euler/Navier-Stokes equations of gas dynamics in general coordinates for both ideal and equilibrium real gases. Also, excellent reviews on modern upwind conservative shock capturing schemes and upwind shock fitting schemes based on wave propagation property have been given by [23-24], respectively.

Traditionally, implicit numerical methods have been praised for their improved stability and condemned for their large arithmetic operation counts ([25]). On the one hand, the slow convergence rate of explicit methods become they so unattractive to the solution of steady state problems due to the large number of iterations required to convergence, in spite of the reduced number of operation counts per time step in comparison with their implicit counterparts. Such problem is resulting from the limited stability region which such methods are subjected (the Courant condition). On the other hand, implicit schemes guarantee a larger stability region, which allows the use of CFL (Currant-Friedrichs-Lewis) numbers above 1.0, and fast convergence to steady state conditions. Undoubtedly, the most significant efficiency achievement for multidimensional implicit methods was the introduction of the Alternating Direction Implicit (ADI) algorithms by [26-28], and fractional step algorithms by [29]. ADI approximate factorization methods consist in approximating the Left Hand Side (LHS) of the numerical scheme by the product of one-dimensional parcels, each one associated with a different spatial coordinate direction, which retract nearly the original implicit operator. These methods have been largely applied in the CFD ("Computational Fluid Dynamics") community and, despite the fact of the error of the approximate factorization, it allows the use of large time steps, which results in significant gains in terms of convergence rate in relation to explicit methods.

In the present work, the [7] TVD symmetric, the [9] TVD symmetric, the [12] TVD, and the [13] TVD/ENO schemes are implemented, on a finite volume context and using a structured spatial discretization, to solve the Euler and Navier-Stokes equations in the three-dimensional space. With the exception of [7; 9], all others schemes are high resolution flux difference splitting ones, based on the concept of Harten's modified flux function. The [7; 9] TVD schemes are symmetrical ones, incorporating TVD properties due to the appropriated definition of a limited dissipation function. All schemes are second order accurate in space. An implicit formulation is employed to solve the Euler equations, whereas a time splitting method, an explicit method, is used to solve the Navier-Stokes equations. An approximate factorization in Linearized Nonconservative Implicit LNI form is employed by the [12-13] schemes, whereas an approximate factorization ADI method is employed by the [7; 9] schemes. All algorithms are first order accurate in time. The algorithms are accelerated to the steady state solution using a spatially variable time step, which has demonstrated effective gains in terms of convergence rate ([30-31]). All schemes are applied to the solution of physical problems of the supersonic shock reflection at the wall and the supersonic flow along a compression corner, in the inviscid case, whereas in the laminar viscous case, the supersonic flow along a compression corner is solved. The results have demonstrated that the [12] algorithm has presented the best solution in the inviscid shock reflection problem; the [13] algorithm, in its ENO version, and the [7] TVD algorithm, in its Van Leer variant, have yielded the best solutions in the inviscid compression corner problem; and the [7] algorithm, in its Minmod1 variant, has presented the best solution in the viscous compression corner problem.

2 Navier-Stokes Equations

As the Euler equations can be obtained from the Navier-Stokes ones by disregarding the viscous vectors, only the formulation to the latter will be presented. The Navier-Stokes equations in integral conservative form, employing a finite volume formulation and using a structured spatial discretization, to three-dimensional simulations, are written as:

$$\partial Q/\partial t + 1/V \int_V \vec{\nabla}\cdot\vec{P}dV = 0\,, \qquad (1)$$

where V is the cell volume, which corresponds to an hexahedron cell in the three-dimensional space; Q is the vector of conserved variables; and $\vec{P} = (E_e - E_v)\vec{i} + (F_e - F_v)\vec{j} + (G_e - G_v)\vec{k}$ represents the complete flux vector in Cartesian coordinates, with the subscript "e" related to the inviscid contributions or the Euler contributions and "v" is related to the viscous contributions. These components of the complete flux vector, as well the vector of conserved variables, are defined as:

$$Q = \begin{Bmatrix} \rho \\ \rho u \\ \rho v \\ \rho w \\ e \end{Bmatrix},\; E_e = \begin{Bmatrix} \rho u \\ \rho u^2 + p \\ \rho uv \\ \rho uw \\ (e+p)u \end{Bmatrix},\; F_e = \begin{Bmatrix} \rho v \\ \rho vu \\ \rho v^2 + p \\ \rho vw \\ (e+p)v \end{Bmatrix};\; (2)$$

$$G_e = \begin{Bmatrix} \rho w \\ \rho wu \\ \rho wv \\ \rho w^2 + p \\ (e+p)w \end{Bmatrix},\; E_v = \frac{1}{\mathrm{Re}}\begin{Bmatrix} 0 \\ \tau_{xx} \\ \tau_{xy} \\ \tau_{xz} \\ \tau_{xx}u + \tau_{xy}v + \tau_{xz}w - q_x \end{Bmatrix};\; (3)$$

$$F_v = \frac{1}{\mathrm{Re}}\begin{Bmatrix} 0 \\ \tau_{yx} \\ \tau_{yy} \\ \tau_{yz} \\ \tau_{yx}u + \tau_{yy}v + \tau_{yz}w - q_y \end{Bmatrix},\; G_v = \frac{1}{\mathrm{Re}}\begin{Bmatrix} 0 \\ \tau_{zx} \\ \tau_{zy} \\ \tau_{zz} \\ \tau_{zx}u + \tau_{zy}v + \tau_{zz}w - q_z \end{Bmatrix}.\; (4)$$

In these equations, the components of the viscous stress tensor are defined as:

$$\tau_{xx} = 2\mu_M\,\partial u/\partial x - 2/3\,\mu_M\left(\partial u/\partial x + \partial v/\partial y + \partial w/\partial z\right);\; (5a)$$

$$\tau_{yy} = 2\mu_M\,\partial v/\partial y - 2/3\,\mu_M\left(\partial u/\partial x + \partial v/\partial y + \partial w/\partial z\right);\; (5b)$$

$$\tau_{zz} = 2\mu_M\,\partial w/\partial z - 2/3\,\mu_M\left(\partial u/\partial x + \partial v/\partial y + \partial w/\partial z\right);\; (5c)$$

$$\tau_{xy} = \tau_{yx} = \mu_M\left(\partial u/\partial y + \partial v/\partial x\right);\qquad (6a)$$

$$\tau_{xz} = \tau_{zx} = \mu_M\left(\partial u/\partial z + \partial w/\partial x\right);\qquad (6b)$$

$$\tau_{yz} = \tau_{zy} = \mu_M\left(\partial v/\partial z + \partial w/\partial y\right);\qquad (6c)$$

The components of the conductive heat flux vector are defined as follows:

$$q_x = -\gamma\left(\mu_M/\mathrm{Pr}\,d\right)\partial e_i/\partial x\,;\qquad (7a)$$

$$q_y = -\gamma\left(\mu_M/\mathrm{Pr}\,d\right)\partial e_i/\partial y\,;\qquad (7b)$$

$$q_z = -\gamma\left(\mu_M/\mathrm{Pr}\,d\right)\partial e_i/\partial z\,.\qquad (7b)$$

The quantities that appear above are described as follows: ρ is the fluid density, u and v are the Cartesian components of the flow velocity vector in the x and y directions, respectively; e is the total energy per unit volume of the fluid; p is the fluid static pressure; e_i is the fluid internal energy, defined as:

$$e_i = e/\rho - 0.5\left(u^2 + v^2 + w^2\right); \quad (8)$$

the τ's represent the components of the viscous stress tensor; Prd is the laminar Prandtl number, which assumed a value of 0.72 in the present simulations; the q's represent the components of the conductive heat flux; μ_M is the fluid molecular viscosity; γ is the ratio of specific heats at constant pressure and volume, respectively, which assumed a value 1.4 to the atmospheric air; and Re is the Reynolds number of the viscous simulation, defined by:

$$\mathrm{Re} = \rho u_{REF} l/\mu_M , \quad (9)$$

where u_{REF} is a characteristic flow velocity and l is a configuration characteristic length. The molecular viscosity is estimated by the empiric Sutherland formula:

$$\mu_M = bT^{1/2}/\left(1 + S/T\right), \quad (10)$$

where T is the absolute temperature (K), b = $1,458\text{x}10^{-6}$ Kg/(m.s.$K^{1/2}$) and S = 110,4 K, to the atmospheric air in the standard atmospheric conditions ([32]). The Navier-Stokes equations were nondimensionalized in relation to the freestream density, ρ_∞, and the freestream speed of sound, a_∞, for the all problems. For the viscous compression corner problem it is also considered the freestream molecular viscosity, μ_∞. To allow the solution of the matrix system of four equations to four unknowns described by Eq. (1), it is employed the state equation of perfect gases presented below:

$$p = (\gamma - 1)\left[e - 0.5\rho(u^2 + v^2 + w^2)\right]. \quad (11)$$

The total enthalpy is determined by:

$$H = (e + p)/\rho . \quad (12)$$

3 Lax and Wendroff Algorithm

The [7] TVD algorithm, second order accurate in space, is specified by the determination of the numerical flux vector at the *(i+½,j,k)* interface. The extension of this numerical flux to the *(i,j+½,k)* and *(i,j,k+½)* interfaces is straightforward, without any additional complications.

The right and left cell volumes, as well the interface volume, necessary to coordinate change, following the finite volume formulation, which is equivalent to a generalized coordinate system, are defined as:

$$V_R = V_{i+1,j,k},\ V_L = V_{i,j,k} \text{ and } V_{\mathrm{int}} = 0.5\left(V_R + V_L\right). \quad (13)$$

The cell volume is calculated according to [33-34]. The metric terms to this generalized coordinate system are defined as:

$$h_x = S_{x\_\mathrm{int}}/V_{\mathrm{int}} ,\ h_y = S_{y\_\mathrm{int}}/V_{\mathrm{int}} ; \quad (14a)$$

$$h_z = S_{z\_\mathrm{int}}/V_{\mathrm{int}} \quad \text{and} \quad h_n = S/V_{\mathrm{int}} , \quad (14b)$$

where $S_{x\_\mathrm{int}} = n_x S$, $S_{y\_\mathrm{int}} = n_y S$, $S_{z\_\mathrm{int}} = n_z S$ are the Cartesian components of the flux area and S is the flux area, calculated as described in [33-34].

The calculated properties at the flux interface are obtained by arithmetical average or by [35] average. The [35] average was used in this work:

$$\rho_{\mathrm{int}} = \sqrt{\rho_L \rho_R},\ u_{\mathrm{int}} = \left(u_L + u_R\sqrt{\rho_R/\rho_L}\right)/\left(1 + \sqrt{\rho_R/\rho_L}\right), \quad (15)$$

$$v_{\mathrm{int}} = \left(v_L + v_R\sqrt{\rho_R/\rho_L}\right)/\left(1 + \sqrt{\rho_R/\rho_L}\right), \quad (16)$$

$$w_{\mathrm{int}} = \left(w_L + w_R\sqrt{\rho_R/\rho_L}\right)/\left(1 + \sqrt{\rho_R/\rho_L}\right); \quad (17)$$

$$H_{\mathrm{int}} = \left(H_L + H_R\sqrt{\rho_R/\rho_L}\right)/\left(1 + \sqrt{\rho_R/\rho_L}\right); \quad (18)$$

$$a_{\mathrm{int}} = \sqrt{(\gamma - 1)\left[H_{\mathrm{int}} - 0.5\left(u_{\mathrm{int}}^2 + v_{\mathrm{int}}^2 + w_{\mathrm{int}}^2\right)\right]}. \quad (19)$$

The eigenvalues of the Euler equations, in the ξ direction, to the convective flux are given by:

$$U_{cont} = u_{\mathrm{int}} h_x + v_{\mathrm{int}} h_y + w_{\mathrm{int}} h_z,\ \lambda_1 = U_{cont} - a_{\mathrm{int}} h_n, \quad (20a)$$

$$\lambda_2 = \lambda_3 = \lambda_4 = U_{cont} \text{ and } \lambda_5 = U_{cont} + a_{\mathrm{int}} h_n . \quad (20b)$$

The jumps in the conserved variables, necessary to the construction of the [7] TVD dissipation function, are given by:-

$$\Delta e = V_{\mathrm{int}}\left(e_R - e_L\right),\ \Delta\rho = V_{\mathrm{int}}\left(\rho_R - \rho_L\right); \quad (21a)$$

$$\Delta(\rho u) = V_{\mathrm{int}}\left[(\rho u)_R - (\rho u)_L\right]; \quad (21b)$$

$$\Delta(\rho v) = V_{\mathrm{int}}\left[(\rho v)_R - (\rho v)_L\right]; \quad (21c)$$

$$\Delta(\rho w) = V_{\mathrm{int}}\left[(\rho w)_R - (\rho w)_L\right], \quad (21d)$$

The α vectors to the *(i+½,j,k)* interface are calculated by the following expressions:

$$\{\alpha_{i+1/2,j,k}\} = [R^{-1}]_{i+1/2,j,k}\{\Delta_{i+1/2,j,k}\overline{Q}\}, \qquad (22)$$

with $[R^{-1}]$ defined according to [36].

The [7] TVD dissipation function is constructed using the right eigenvector matrix of the Jacobian matrix in the normal direction to the flux face. This matrix is also defined in [36].

According to [9], five different limiters are implemented which incorporate the TVD properties to the original [7] scheme. The limited dissipation function Q is defined to the five options as:

$$Q(r^-,r^+) = min\,mod(1,r^-) + min\,mod(1,r^+) - 1; \qquad (23)$$

$$Q(r^-,r^+) = min\,mod(1,r^-,r^+); \qquad (24)$$

$$Q(r^-,r^+) = min\,mod[2,2r^-,2r^+,0{,}5(r^-+r^+)]; \qquad (25)$$

$$\mathrm{Q}(\mathrm{r}^-,\mathrm{r}^+) = \mathrm{MAX}[0,\mathrm{MIN}(2\mathrm{r}^-,1),\mathrm{MIN}(\mathrm{r}^-,2)] + \mathrm{MAX}[0,\mathrm{MIN}(2\mathrm{r}^+,1),\mathrm{MIN}(\mathrm{r}^+,2)] - 1; \qquad (26)$$

$$Q(r^-,r^+) = \frac{r^- + |r^-|}{1+r^-} + \frac{r^+ + |r^+|}{1+r^+} - 1, \qquad (27)$$

where:

$$\left(r^-_{i+1/2,j,k}\right)^l = \alpha^l_{i-1/2,j,k} / \alpha^l_{i+1/2,j,k}; \qquad (28)$$

$$\left(r^+_{i+1/2,j,k}\right)^l = \alpha^l_{i+3/2,j,k} / \alpha^l_{i+1/2,j,k}, \qquad (29)$$

"*l*" assuming values from 1 to 5. Equations (23) to (25) are referenced by these authors as Minmod1, Minmod2 and Minmod3, respectively. Equation (26) is referred in the CFD literature as the "Super Bee" limiter due to [37] and Eq. (27) is referred as the Van Leer limiter due to [38].

The [7] TVD dissipation function is finally constructed by the following matrix-vector product:

$$\{D_{LW}\}_{i+1/2,j,k} = [R]_{i+1/2,j,k}\{[\Delta t_{i,j,k}\lambda^2 Q + |\lambda|(1-Q)]\alpha\}_{i+1/2,j,k}. \qquad (30)$$

The complete numerical flux vector to the *(i+½,j,k)* interface is described by:

$$F^{(l)}_{i+1/2,j,k} = \left(E^{(l)}_{\mathrm{int}}h_x + F^{(l)}_{\mathrm{int}}h_y + G^{(l)}_{\mathrm{int}}h_z\right)V_{\mathrm{int}} - 0.5D^{(l)}_{LW}, \qquad (31)$$

with:

$$E^{(l)}_{int} = 0.5\left[\left(E^{(l)}_R + E^{(l)}_L\right)_e\right] - \left(E^{(l)}_v\right)_{int}; \qquad (32)$$

$$F^{(l)}_{int} = 0.5\left[\left(F^{(l)}_R + F^{(l)}_L\right)_e\right] - \left(F^{(l)}_v\right)_{int}. \qquad (33)$$

$$G^{(l)}_{\mathrm{int}} = 0.5\left[\left(G^{(l)}_R + G^{(l)}_L\right)_e\right] - \left(G^{(l)}_v\right)_{\mathrm{int}}. \qquad (34)$$

The viscous vectors at the flux interface are obtained by arithmetical average between the primitive variables at the left and at the right states of the flux interface, as also arithmetical average of the primitive variable gradients also considering the left and the right states of the flux interface.

The right-hand-side (RHS) of the [7] TVD scheme, necessaries to the resolution of the implicit version of this algorithm, is determined by:

$$RHS(LW)^n_{i,j,k} = -\Delta t_{i,j,k}/V_{i,j,k}\left[F^{LW}_{i+1/2,j,k} - F^{LW}_{i-1/2,j,k} + F^{LW}_{i+1/2,j,k} - F^{LW}_{i-1/2,j,k} + F^{LW}_{i,j,k+1/2} - F^{LW}_{i,j,k-1/2}\right]^n. \qquad (35)$$

The time integration to the viscous simulations follows the time splitting method, first order accurate, which divides the integration in three steps, each one associated with a specific spatial direction. In the initial step, it is possible to write for the ξ direction:

$$\Delta Q^*_{i,j,k} = -\Delta t_{i,j,k}/V_{i,j,k}\left(F^n_{i+1/2,j,k} - F^n_{i-1/2,j,k}\right);$$
$$Q^*_{i,j,k} = Q^n_{i,j,k} + \Delta Q^*_{i,j,k}; \qquad (36)$$

in the intermediate step, η direction:

$$\Delta Q^{**}_{i,j,k} = -\Delta t_{i,j,k}/V_{i,j,k}\left(F^*_{i,j+1/2,k} - F^*_{i,j-1/2,k}\right);$$
$$Q^{**}_{i,j,k} = Q^*_{i,j,k} + \Delta Q^{**}_{i,j,k}. \qquad (37)$$

and at the final step, ζ direction:

$$\Delta Q^{n+1}_{i,j,k} = -\Delta t_{i,j,k}/V_{i,j,k}\left(F^{**}_{i,j,k+1/2} - F^{**}_{i,j,k-1/2}\right);$$
$$Q^{n+1}_{i,j,k} = Q^{**}_{i,j,k} + \Delta Q^{n+1}_{i,j,k}. \qquad (38)$$

4 Yee, Warming and Harten Algorithm

The [12] numerical algorithm, second order accurate in space, is specified by the determination of the numerical flux vector at the *(i+½,j,k)* interface. This scheme employs Eqs. (13-22). The g numerical flux function, which is a limited function to avoid the formation of new extrema in the solution and is responsible by the second order spatial precision of the scheme, is defined by:

$$g^l_{i,j,k} = signal_l \times MAX\left[0.0; MIN\left(\sigma^l_{i+1/2,j,k}\left|\alpha^l_{i+1/2,j,k}\right|,\right.\right.$$
$$\left.\left. signal_l \times \sigma^l_{i-1/2,j,k}\alpha^l_{i-1/2,j,k}\right)\right], \quad (39)$$

where $signal_l$ is equal to 1.0 if $\alpha^l_{i+1/2,j,k} \geq 0.0$ and -1.0 otherwise; $\sigma^l(\lambda_l) = 0.5Q_l(\lambda_l)$; and Q, the entropy function, is defined as:

$$Q_l(W_l) = \begin{cases} |W_l|, & if\ |W_l| \geq \delta_f \\ 0.5\left(W_l^2 + \delta_f^2\right)/\delta_f, & if\ |W_l| < \delta_f \end{cases}, \quad (40)$$

where "*l*" varies from 1 to 5 (three-dimensional space) and δ_f assuming values between 0.1 and 0.5, being 0.2 the value recommended by [12].

The θ term, responsible by artificial compressibility, which improves the scheme resolution in discontinuities like shock wave and contact discontinuities, is defined by

$$\theta^l_{i,j,k} = \begin{cases} \left|\alpha^l_{i+1/2,j,k} - \alpha^l_{i-1/2,j,k}\right| / \left(\left|\alpha^l_{i+1/2,j,k}\right| + \left|\alpha^l_{i-1/2,j,k}\right|\right), & if\ \left|\alpha^l_{i+1/2,j,k}\right| + \left|\alpha^l_{i-1/2,j,k}\right| \neq 0.0 \\ 0.0, & if\ \left|\alpha^l_{i+1/2,j,k}\right| + \left|\alpha^l_{i-1/2,j,k}\right| = 0.0 \end{cases}; \quad (41)$$

The β parameter at the *(i+½,j,k)* interface, which introduces the artificial compressibility term in the algorithm, is given by the following expression:

$$\beta_l = 1.0 + \omega_l \theta^l_{i,j,k}, \quad (42)$$

in which ω_l assumes the following values: $\omega_1 = \omega_5 = 0.25$ (non-linear fields) and $\omega_2 = \omega_3 = \omega_4 = 1.0$ (linear fields). The $\tilde{g}$ function is defined by:

$$\tilde{g}^l_{i,j} = \beta_l g^l_{i,j,k}. \quad (43)$$

The numerical characteristic velocity, φ_l, at the *(i+½,j,k)* interface, which is responsible by the transport of numerical information associated with the numerical flux function g, or indirectly through the $\tilde{g}$, is defined by:

$$\varphi_l = \begin{cases} \left(\tilde{g}^l_{i+1,j,k} - \tilde{g}^l_{i,j,k}\right)/\alpha^l, & if\ \alpha^l \neq 0.0 \\ 0.0, & if\ \alpha^l = 0.0 \end{cases}. \quad (44)$$

Finally, the [12] dissipation function, to second order spatial accuracy, is constructed by the following matrix-vector product:

$$\{D_{YWH/85}\}_{i+1/2,j,k} = [R]_{i+1/2,j,k}\left\{\left(g_{i,j,k} + g_{i+1,j,k}\right) - Q(\lambda + \varphi)\alpha\right\}_{i+1/2,j,k}. \quad (45)$$

The numerical flux vector at the *(i+½,j,k)* interface is described by:

$$F^{(l)}_{i+1/2,j,k} = \left(E^{(l)}_{int}h_x + F^{(l)}_{int}h_y + G^{(l)}_{int}h_z\right)V_{int} + 0.5D^{(l)}_{YWH/85}. \quad (46)$$

The Equations (32-34) are employed to conclude the numerical flux vector of the [12] scheme and the time marching is performed by the implicit ADI factorization to be discussed in section 7. The RHS to this scheme is defined as:

$$RHS(YWH)^n_{i,j,k} = -\Delta t_{i,j,k}/V_{i,j,k}\left[F^{YWH}_{i+1/2,j,k} - F^{YWH}_{i-1/2,j,k} + F^{YWH}_{i,j+1/2,k} - F^{YWH}_{i,j-1/2,k} + F^{YWH}_{i,j,k+1/2} - F^{YWH}_{i,j,k-1/2}\right]^n. \quad (47)$$

The time splitting method, defined by Eqs. (36-38), is employed to the explicit viscous simulations.

5 Yee Algorithm

The symmetric TVD scheme of [9], second order accurate in space, employs the Eqs. (13-29). The dissipation function to the [9] symmetric TVD scheme is defined as follows:

$$\left(\phi^l_{i+1/2,j,k}\right)_{Yee} = \Psi\left(\lambda^l_{i+1/2,j,k}\right)\left(1 - Q^l_{i+1/2,j,k}\right)\alpha^l_{i+1/2,j,k}, \quad (48)$$

with the Ψ entropy function defined by:

$$\Psi(z) = \begin{cases} |z|, & if\ |z| \geq \varepsilon \\ \left(z^2 + \varepsilon^2\right)/2\varepsilon, & if\ |z| < \varepsilon \end{cases}, \quad (49)$$

where z, ε are scalars.

The [9] TVD dissipation function is finally constructed by the following matrix-vector product:

$$\{D_{Yee}\}_{i+1/2,j,k} = [R]_{i+1/2,j,k}\{\phi_{Yee}\}_{i+1/2,j,k}, \quad (50)$$

The complete numerical flux vector to the *(i+½,j,k)* interface is described by:

$$F^{(l)}_{i+1/2,j,k} = \left(E^{(l)}_{int}h_x + F^{(l)}_{int}h_y + G^{(l)}_{int}h_z\right)V_{int} - 0.5D^{(l)}_{Yee}, \quad (51)$$

with $E^{(l)}_{int}$, $F^{(l)}_{int}$ and $G^{(l)}_{int}$ defined according to Eqs. (32-34). The viscous terms are calculated in the same way as described in section 3.

The right-hand-side (RHS) of the [9] TVD symmetric scheme, necessaries to the resolution of the implicit version of this algorithm, is defined by:

$$RHS(Yee)^n_{i,j,k} = -\Delta t_{i,j,k}/V_{i,j,k}\left[F^{Yee}_{i+1/2,j,k} - F^{Yee}_{i-1/2,j,k} + F^{Yee}_{i,j+1/2,k} - F^{Yee}_{i,j-1/2,k} + F^{Yee}_{i,j,k+1/2} - F^{Yee}_{i,j,k-1/2}\right]^n. \quad (52)$$

The explicit version to the viscous simulations is defined by Eqs. (36-38).

6 Harten and Osher Algorithm

The [13] algorithm, second order accurate in space, employs Eqs. (13-22). The next step consists in constructing the TVD/ENO numerical flux vector.

Initially, it is necessary to define the σ parameter at the *(i+½,j,k)* interface to calculate the numerical velocity of information propagation, which contributes to the second order spatial accuracy of the scheme:

$$\sigma(z) = 0.5\left[\Psi(z) - \Delta t_{i,j,k} z^2\right]; \quad (53)$$

with Ψ(z) defined according to Eq. (49). The non-linear limited flux function, based on the idea of a modified flux function of [3], is constructed by:

$$\overline{\beta}^{l}_{i,j,k} = m\left[\alpha^{l}_{i+1/2,j,k} - \zeta\overline{m}\left(\Delta_+\alpha^{l}_{i+1/2,j,k}, \Delta_-\alpha^{l}_{i+1/2,j,k}\right),\right.$$
$$\left.\alpha^{l}_{i-1/2,j,k} + \zeta\overline{m}\left(\Delta_+\alpha^{l}_{i-1/2,j,k}, \Delta_-\alpha^{l}_{i-1/2,j,k}\right)\right], \quad (54)$$

where the m and $\overline{m}$ limiters are defined as:

$$m(y,z) = \begin{cases} s \times MIN(|y|,|z|), & if\ signal(y) = signal(z) = s \\ 0, & otherwise \end{cases}; \quad (55)$$

$$\overline{m}(y,z) = \begin{cases} y, & if\ |y| \le |z| \\ z, & if\ |y| > |z| \end{cases}; \quad (56)$$

and the forward and backward operators are defined according to:

$$\Delta_+ = (\cdot)_{i+1,j,k} - (\cdot)_{i,j,k} \text{ and } \Delta_- = (\cdot)_{i,j,k} - (\cdot)_{i-1,j,k}. \quad (57)$$

The numerical velocity of information propagation is calculated by:

$$\overline{\gamma}^{l}_{i+1/2,j,k} = \sigma\left(\lambda^{l}_{i+1/2,j,k}\right)\begin{cases} \left(\overline{\beta}^{l}_{i+1,j,k} - \overline{\beta}^{l}_{i,j,k}\right)/\alpha^{l}_{i+1/2,j,k}, & if\ \alpha^{l}_{i+1/2,j,k} \ne 0; \\ 0, & otherwise. \end{cases} \quad (58)$$

The dissipation function to the TVD and ENO versions of the [13] scheme is defined as:

$$\left(\phi^{l}_{i+1/2,j,k}\right)_{HO} = \sigma\left(\lambda^{l}_{i+1/2,j,k}\right)\left(\overline{\beta}^{l}_{i,j,k} + \overline{\beta}^{l}_{i+1,j,k}\right) - \Psi\left(\lambda^{l}_{i+1/2,j,k} + \overline{\gamma}^{l}_{i+1/2,j,k}\right)$$
$$\alpha^{l}_{i+1/2,j,k}, \quad (59)$$

with: "l" assuming values from 1 to 5 (three-dimensional space), ε assuming the value 0.2 recommended by [13], Ψ is the entropy function to guarantee that only relevant physical solutions are admissible, and ζ assumes the value 0.0 to obtain the TVD scheme of [3], second order accurate, and 0.5 to obtain the essentially non-oscillatory scheme, uniform second order accuracy in the field, of [13].

Finally, the dissipation operator of [13], to second order of spatial accuracy, in its TVD and ENO versions, is constructed by the following matrix-vector product:

$$\{D_{HO}\}_{i+1/2,j,k} = [R]_{i+1/2,j,k}\{\phi_{HO}\}_{i+1/2,j,k}. \quad (60)$$

The complete numerical flux vector to the *(i+½,j,k)* interface is described by:

$$F^{(l)}_{i+1/2,j,k} = \left(E^{(l)}_{int}h_x + F^{(l)}_{int}h_y + G^{(l)}_{int}h_z\right)V_{int} + 0.5D^{(l)}_{HO}, \quad (61)$$

with $E^{(l)}_{int}$, $F^{(l)}_{int}$ and $G^{(l)}_{int}$ defined according to Eqs. (32-34). The viscous terms are calculated in the same way as described in section 3.

The RHS of the [13] algorithm, necessaries to the resolution of the implicit version of this scheme, is determined by:

$$RHS(HO)^n_{i,j,k} = -\Delta t_{i,j,k}/V_{i,j,k}\left[F^{HO}_{i+1/2,j,k} - F^{HO}_{i-1/2,j,k} + \right.$$
$$\left.F^{HO}_{i,j+1/2,k} - F^{HO}_{i,j-1/2,k} + F^{HO}_{i,j,k+1/2} - F^{HO}_{i,j,k-1/2}\right]^n. \quad (62)$$

The explicit version to the viscous simulations employs a time splitting method, first order accurate in time, which divides the integration in three parts, each one associated with a specific spatial direction. This explicit version is defined by Eqs. (36-38).

7 Implicit Formulations

All schemes tested in this work employed an ADI formulation to solve the system of non-linear algebraic equations. Initially, the system of non-linear equations is linearized considering the implicit operator evaluated at time "n" and, posteriorly, the five-diagonal system of linear algebraic equations is factored in two systems of three-diagonal linear algebraic equations, each one associated with a particular spatial direction. The Thomas algorithm is employed to solve the two three-diagonal systems. The implicit formulation is employed to solve only the Euler equations, which implies that only the convective flux contributions are taken into account.

All implemented schemes used the backward Euler method and an ADI or LNI approximate factorization to solve the three-diagonal system in each direction.

7.1 Implicit Scheme to the TVD symmetric algorithms of [7] and [9]

An ADI form of the implicit TVD symmetric algorithms of [7] and [9] is represented by:

$$E_1\Delta Q^*_{i-1,j,k} + E_2\Delta Q^*_{i,j,k} + E_3\Delta Q^*_{i+1,j,k} = [RHS]^n_{i,j,k},$$

to the ξ direction; (63)

$$F_1\Delta Q^{**}_{i,j-1,k} + F_2\Delta Q^{**}_{i,j,k} + F_3\Delta Q^{**}_{i,j+1,k} = \Delta Q^*_{i,j,k}, \quad (64)$$

to the η direction;

$$G_1\Delta Q^{n+1}_{i,j,k-1} + G_2\Delta Q^{n+1}_{i,j,k} + G_3\Delta Q^{n+1}_{i,j,k+1} = \Delta Q^{**}_{i,j,k}, \quad (65)$$

to the ζ direction;

$$Q^{n+1}_{i,j} = Q^n_{i,j} + \Delta Q^{n+1}_{i,j}, \quad (66)$$

where:

$$E_1 = \frac{\Delta t_{i,j,k}\theta}{2}\left(-A_{i-1/2,j,k} - K_{i-1/2,j,k}\right)^n; \quad (67)$$

$$E_2 = I + \frac{\Delta t_{i,j,k}\theta}{2}\left(K_{i-1/2,j,k} + K_{i+1/2,j,k}\right)^n; \quad (68)$$

$$E_3 = \frac{\Delta t_{i,j,k}\theta}{2}\left(A_{i+1/2,j,k} - K_{i+1/2,j,k}\right)^n; \quad (69)$$

$$F_1 = \frac{\Delta t_{i,j,k}\theta}{2}\left(-B_{i,j-1/2,k} - J_{i,j-1/2,k}\right)^n; \quad (70)$$

$$F_2 = I + \frac{\Delta t_{i,j,k}\theta}{2}\left(J_{i,j-1/2,k} + J_{i,j+1/2,k}\right)^n; \quad (71)$$

$$F_3 = \frac{\Delta t_{i,j,k}\theta}{2}\left(B_{i,j+1/2,k} - J_{i,j+1/2,k}\right)^n; \quad (72)$$

$$G_1 = \frac{\Delta t_{i,j,k}\theta}{2}\left(-C_{i,j,k-1/2} - L_{i,j,k-1/2}\right)^n; \quad (73)$$

$$G_2 = I + \frac{\Delta t_{i,j,k}\theta}{2}\left(L_{i,j,k-1/2} + L_{i,j,k+1/2}\right)^n; \quad (74)$$

$$G_3 = \frac{\Delta t_{i,j,k}\theta}{2}\left(C_{i,j,k+1/2} - L_{i,j,k+1/2}\right)^n; \quad (75)$$

$$A^n_{i\pm1/2,j,k} = [R]^n_{i\pm1/2,j,k}\, diag\left(\lambda^l_\xi\right)^n_{i\pm1/2,j,k}\left[R^{-1}\right]^n_{i\pm1/2,j,k}; \quad (76)$$

$$B^n_{i,j\pm1/2,k} = [R]^n_{i,j\pm1/2,k}\, diag\left(\lambda^l_\eta\right)^n_{i,j\pm1/2,k}\left[R^{-1}\right]^n_{i,j\pm1/2,k}; \quad (77)$$

$$C^n_{i,j,k\pm1/2} = [R]^n_{i,j,k\pm1/2}\, diag\left(\lambda^l_\zeta\right)^n_{i,j,k\pm1/2}\left[R^{-1}\right]^n_{i,j,k\pm1/2}; \quad (78)$$

$$K^n_{i\pm1/2,j,k} = [R]^n_{i\pm1/2,j,k}\,\Omega^n_{i\pm1/2,j,k}\left[R^{-1}\right]^n_{i\pm1/2,j,k}; \quad (79)$$

$$J^n_{i,j\pm1/2,k} = [R]^n_{i,j\pm1/2,k}\,\Phi^n_{i,j\pm1/2,k}\left[R^{-1}\right]^n_{i,j\pm1/2,k}; \quad (80)$$

$$L^n_{i,j,k\pm1/2} = [R]^n_{i,j,k\pm1/2}\,\Theta^n_{i,j,k\pm1/2}\left[R^{-1}\right]^n_{i,j,k\pm1/2}; \quad (81)$$

$$\Omega^n_{i\pm1/2,j,k} = diag\left[\Psi\left(\lambda^l_\xi\right)\right]^n_{i\pm1/2,j,k}; \quad (82)$$

$$\Phi^n_{i,j\pm1/2,k} = diag\left[\Psi\left(\lambda^l_\eta\right)\right]^n_{i,j\pm1/2,k}; \quad (83)$$

$$\Theta^n_{i,j,k\pm1/2} = diag\left[\Psi\left(\lambda^l_\zeta\right)\right]^n_{i,j,k\pm1/2}. \quad (84)$$

In Equations (76-81), the R and R^{-1} matrices are defined according to [36], applied to each coordinate direction; in Eqs. (76-78) and (82-84), "*l*" assumes values from 1 to 5 (three-dimensional space); and the interface properties are calculated by the [33] average. The RHS operator is defined by Eq. (35) if the [7] algorithm is solved and by Eq. (52) if the [9] algorithm is solved.

This implementation is first order accurate in time due to Ω, Φ and Θ definitions, as reported by [9]. The θ parameter defines the time integration method to be employed. A 0.0 value to this parameter results in the Euler explicit method; the value 0.5 implies in the trapezoidal method; and the value 1.0 results in the backward Euler method. In the present study, the backward Euler method was used. During the iterative process and at the steady state conditions, this implementation results, due to the employed non-linear limiters, in second order TVD algorithms.

7.2 Implicit Scheme to the TVD and ENO algorithms of [12] and [13]

In the flux difference splitting cases, the [12-13] algorithms, a Linearized Nonconservative Implicit form is applied which, although the resulting schemes lose the conservative property, they preserve their unconditional TVD properties. Moreover, the LNI form is mainly useful to steady state problems where the conservative property is recovery by these schemes in this condition. This LNI form was proposed by [12].

The LNI form is defined by the following two step algorithm:

$$\left[I - \Delta t_{i,j,k} J^-_{i+1/2,j,k}\Delta_{i+1/2,j,k} + \Delta t_{i,j,k} J^+_{i-1/2,j,k}\Delta_{i-1/2,j,k}\right]\Delta Q^*_{i,j,k} = [RHS]^n_{i,j,k},$$

in the ξ direction; (85)

$$\left[I - \Delta t_{i,j,k} K^-_{i,j+1/2,k}\Delta_{i,j+1/2,k} + \Delta t_{i,j,k} K^+_{i,j-1/2,k}\Delta_{i,j-1/2,k}\right]\Delta Q^{**}_{i,j,k} = \Delta Q^*_{i,j,k},$$

in the η direction; (86)

$$\left[I - \Delta t_{i,j,k} L^{-}_{i,j,k+1/2} \Delta_{i,j,k+1/2} + \Delta t_{i,j,k} L^{+}_{i,j,k-1/2} \Delta_{i,j,k-1/2}\right] \Delta Q^{n+1}_{i,j,k} =$$

$\Delta Q^{**}_{i,j,k}$, in the ζ direction; (86)

$$Q^{n+1}_{i,j} = Q^{n}_{i,j} + \Delta Q^{n+1}_{i,j}, \quad (87)$$

where RHS is defined by Eq. (47) if the [12] scheme is being solved, or (62), if the [13] scheme is being solved. The difference operators are defined as:

$$\Delta_{i+1/2,j,k}(\cdot) = (\cdot)_{i+1,j,k} - (\cdot)_{i,j,k}, \quad \Delta_{i-1/2,j,k}(\cdot) = (\cdot)_{i,j,k} - (\cdot)_{i-1,j,k}; \quad (88a)$$

$$\Delta_{i,j+1/2,k}(\cdot) = (\cdot)_{i,j+1,k} - (\cdot)_{i,j,k}, \quad \Delta_{i,j-1/2,k}(\cdot) = (\cdot)_{i,j,k} - (\cdot)_{i,j-1,k}; \quad (88b)$$

$$\Delta_{i,j,k+1/2}(\cdot) = (\cdot)_{i,j,k+1} - (\cdot)_{i,j,k}, \quad \Delta_{i,j,k-1/2}(\cdot) = (\cdot)_{i,j,k} - (\cdot)_{i,j,k-1}; \quad (88c)$$

As aforementioned, this three-diagonal linear system, composed of a 5x5 block matrices, is solved using LU decomposition and the Thomas algorithm, defined by a block matrix system.

The separated matrices J^{+}, J^{-}, K^{+}, K^{-}, L^{+} and L^{-} are defined as follows:

$$J^{+} = R_{\xi}\, diag\left(D^{+}_{\xi}\right) R^{-1}_{\xi},\; J^{-} = R_{\xi}\, diag\left(D^{-}_{\xi}\right) R^{-1}_{\xi}, \quad (89)$$

$$K^{+} = R_{\eta}\, diag\left(D^{+}_{\eta}\right) R^{-1}_{\eta},\; K^{-} = R_{\eta}\, diag\left(D^{-}_{\eta}\right) R^{-1}_{\eta}, \quad (90)$$

$$L^{+} = R_{\zeta}\, diag\left(D^{+}_{\zeta}\right) R^{-1}_{\zeta},\; L^{-} = R_{\zeta}\, diag\left(D^{-}_{\zeta}\right) R^{-1}_{\zeta}, \quad (91)$$

in which the R_{ξ}, R_{η} and R_{ζ} matrices are defined according to [36] applied to the respective coordinate; and R^{-1}_{ξ} , R^{-1}_{η} and R^{-1}_{ζ} defined according to [36] applied to the respective coordinate direction.

The diagonal matrices of the [12-13] schemes are determined by:

$$diag\left(D^{+}_{\xi}\right) = \begin{bmatrix} D^{\xi,+}_{1} & & & & \\ & D^{\xi,+}_{2} & & & \\ & & D^{\xi,+}_{3} & & \\ & & & D^{\xi,+}_{4} & \\ & & & & D^{\xi,+}_{5} \end{bmatrix} \text{ and}$$

$$diag\left(D^{-}_{\xi}\right) = \begin{bmatrix} D^{\xi,-}_{1} & & & & \\ & D^{\xi,-}_{2} & & & \\ & & D^{\xi,-}_{3} & & \\ & & & D^{\xi,-}_{4} & \\ & & & & D^{\xi,-}_{5} \end{bmatrix} \quad (92)$$

with the D terms expressed as

$$D^{\pm}_{\xi} = 0.5\left[\Psi\left(\lambda^{l}_{\xi} + \gamma^{l}_{\xi}\right) \pm \left(\lambda^{l}_{\xi} + \gamma^{l}_{\xi}\right)\right];$$

$$D^{\pm}_{\eta} = 0.5\left[\Psi\left(\lambda^{l}_{\eta} + \gamma^{l}_{\eta}\right) \pm \left(\lambda^{l}_{\eta} + \gamma^{l}_{\eta}\right)\right];$$

$$D^{\pm}_{\zeta} = 0.5\left[\Psi\left(\lambda^{l}_{\zeta} + \gamma^{l}_{\zeta}\right) \pm \left(\lambda^{l}_{\zeta} + \gamma^{l}_{\zeta}\right)\right], \quad (93)$$

where:

Ψ defined by Eq. (49);

λ^{l}_{ξ}, λ^{l}_{η} and λ^{l}_{ζ} are the eigenvalues of the Euler equations, determined by Eqs. (20a-20b), in each coordinate direction;

$$\left(\gamma^{l}_{\xi}\right)_{i+1/2,j,k} = \begin{cases} \left[\left(g'_{\xi}\right)^{l}_{i+1,j,k} - \left(g'_{\xi}\right)^{l}_{i,j,k}\right] \Big/ \left(\alpha^{l}_{\xi}\right)_{i+1/2,j,k}, & \text{if } \left(\alpha^{l}_{\xi}\right)_{i+1/2,j,k} \neq 0.0 \\ 0.0, & \text{if } \left(\alpha^{l}_{\xi}\right)_{i+1/2,j,k} = 0.0 \end{cases}; \quad (94)$$

$$\left(\gamma^{l}_{\eta}\right)_{i,j+1/2,k} = \begin{cases} \left[\left(g'_{\eta}\right)^{l}_{i,j+1,k} - \left(g'_{\eta}\right)^{l}_{i,j,k}\right] \Big/ \left(\alpha^{l}_{\eta}\right)_{i,j+1/2,k}, & \text{if } \left(\alpha^{l}_{\eta}\right)_{i,j+1/2,k} \neq 0.0 \\ 0.0, & \text{if } \left(\alpha^{l}_{\eta}\right)_{i,j+1/2,k} = 0.0 \end{cases}; \quad (95)$$

$$\left(\gamma^{l}_{\zeta}\right)_{i,j,k+1/2} = \begin{cases} \left[\left(g'_{\zeta}\right)^{l}_{i,j,k+1} - \left(g'_{\zeta}\right)^{l}_{i,j,k}\right] \Big/ \left(\alpha^{l}_{\zeta}\right)_{i,j,k+1/2}, & \text{if } \left(\alpha^{l}_{\zeta}\right)_{i,j,k+1/2} \neq 0.0 \\ 0.0, & \text{if } \left(\alpha^{l}_{\zeta}\right)_{i,j,k+1/2} = 0.0 \end{cases}; \quad (96)$$

$$\left(g'_{\xi}\right)^{l}_{i,j,k} = \text{signal}^{l}_{\xi} \text{MAX}\left[0.0, \text{MIN}\left(\sigma^{l}_{i+1/2,j,k}\left|\left(\alpha^{l}_{\xi}\right)_{i+1/2,j,k}\right|, \text{signal}^{l}_{\xi}\sigma^{l}_{i-1/2,j,k}\left(\alpha^{l}_{\xi}\right)_{i-1/2,j,k}\right)\right]; \quad (97)$$

$$\left(g'_{\eta}\right)^{l}_{i,j,k} = \text{signal}^{l}_{\eta} \text{MAX}\left[0.0, \text{MIN}\left(\sigma^{l}_{i,j+1/2,k}\left|\left(\alpha^{l}_{\eta}\right)_{i,j+1/2,k}\right|, \text{signal}^{l}_{\eta}\sigma^{l}_{i,j-1/2,k}\left(\alpha^{l}_{\eta}\right)_{i,j-1/2,k}\right)\right]; \quad (98)$$

$$\left(g'_{\zeta}\right)^{l}_{i,j,k} = \text{signal}^{l}_{\zeta} \text{MAX}\left[0.0, \text{MIN}\left(\sigma^{l}_{i,j,k+1/2}\left|\left(\alpha^{l}_{\zeta}\right)_{i,j,k+1/2}\right|, \text{signal}^{l}_{\zeta}\sigma^{l}_{i,j,k-1/2}\left(\alpha^{l}_{\zeta}\right)_{i,j,k-1/2}\right)\right]; \quad (99)$$

$\sigma^{l} = 1/2\,\Psi^{l}\left(\lambda^{l}\right)$ to steady state simulations. (100)

Finally, signal^{l}_{ξ} = 1.0 if $\left(\alpha^{l}_{\xi}\right)_{i+1/2,j,k} \geq 0.0$ and -1.0 otherwise; signal^{l}_{η} = 1.0 if $\left(\alpha^{l}_{\eta}\right)_{i,j+1/2,k} \geq 0.0$ and -1.0 otherwise; and $\text{signal}^{l}_{\zeta}$ = 1.0 if $\left(\alpha^{l}_{\zeta}\right)_{i,j,k+1/2} \geq 0.0$ and -1.0 otherwise.

This implicit formulation to the LHS of the TVD scheme of [12] and TVD/ENO scheme of [13] is second order accurate in space and first order accurate in time due to the presence of the characteristic numerical speed γ associated with the numerical flux function g'. In this case, the algorithms accuracy is definitely second order in space because both LHS and RHS are second order accurate.

It is important to emphasize that the RHS of the flux difference splitting implicit schemes present steady state solutions which depend of the time step. With this behavior, the use of large time steps can affect the stationary solutions, as mentioned in [39]. This is an initial study with implicit schemes and improvements in the numerical implementation of these algorithms with steady state solutions independent of the time step is a goal to be reached in future work of both authors.

8 Spatially Variable Time Step

The basic idea of this procedure consists in keeping constant the CFL number in all calculation domain, allowing, hence, the use of appropriated time steps to each specific mesh region during the convergence process. According to the definition of the CFL number, it is possible to write:

$$\Delta t_{i,j,k} = CFL(\Delta s)_{i,j,k} / c_{i,j,k} , \qquad (101)$$

where CFL is the "Courant-Friedrichs-Lewy" number to provide numerical stability to the scheme; $c_{i,j,k} = \left[\left(u^2 + v^2 + w^2\right)^{0.5} + a\right]_{i,j,k}$ is the maximum characteristic speed of information propagation in the calculation domain; and $(\Delta s)_{i,j,k}$ is a characteristic length of information transport. On a finite volume context, $(\Delta s)_{i,j,k}$ is chosen as the minor value found between the minor barycenter distance, involving the *(i,j,k)* cell and a neighbor, and the minor cell side length.

9 Initial and Boundary Conditions

9.1 Initial Condition

To the physical problems studied in this work, freestream flow values are adopted for all properties as initial condition, in the whole calculation domain ([33;40]). Therefore, the vector of conserved variables is defined as:

$$Q_{i,j} = \left\{1 \quad M_\infty \cos\alpha \quad M_\infty \sin\alpha \quad \frac{1}{\gamma(\gamma-1)} + 0.5M_\infty^2\right\}^T ,$$

being α the flow attack angle. (102)

9.2 Boundary Conditions

The boundary conditions are basically of four types: solid wall, entrance, exit and lateral frontiers. The far field condition is a case of entrance and exit frontiers. These conditions are implemented in special cells named ghost cells.

(a) Wall condition: This condition imposes the flow tangency at the solid wall. This condition is satisfied considering the wall tangent velocity component of the ghost volume as equals to the respective velocity component of its real neighbor cell. At the same way, the wall normal velocity component of the ghost cell is equaled in value, but with opposite signal, to the respective velocity component of the real neighbor cell. According to [41], it results in:

$$u_g = (1 - 2n_x n_x)u_{real} + (-2n_x n_y)v_{real} + (-2n_x n_z)w_{real} ; \qquad (103)$$

$$v_g = (-2n_y n_x)u_{real} + (1 - 2n_y n_y)v_{real} + (-2n_y n_z)w_{real} ; \qquad (104)$$

$$w_g = (-2n_z n_x)u_{real} + (-2n_z n_y)v_{real} + (1 - 2n_z n_z)w_{real} , \qquad (105)$$

with "g" related with ghost cell and "r" related with real cell. To the viscous case, the boundary condition imposes that the ghost cell velocity components be equal to the real cell velocity components, with the negative signal:

$$u_g = -u_{real}; \qquad (106)$$

$$v_g = -v_{real}, \qquad (107)$$

$$w_g = -w_{real}. \qquad (108)$$

The pressure gradient normal to the wall is assumed be equal to zero, following an inviscid formulation and according to the boundary layer theory. The same hypothesis is applied to the temperature gradient normal to the wall, considering adiabatic wall. The ghost volume density and pressure are extrapolated from the respective values of the real neighbor volume (zero order extrapolation), with these two conditions. The total energy is obtained by the state equation of a perfect gas.

(b) Entrance condition:

(b.1) Subsonic flow: Four properties are specified and one is extrapolated, based on analysis of information propagation along characteristic directions in the calculation domain ([33]). In other words, four characteristic directions of information propagation point inward the computational domain and should be specified. Only the characteristic direction associated to the "$(q_n\text{-}a)$" velocity cannot be specified and should be determined by interior information of the calculation domain. The pressure was the extrapolated variable from the real neighbor volume, to the studied problems. Density and velocity components had their values determined by the freestream flow properties. The total energy per unity fluid volume is determined by the state equation of a perfect gas.

(b.2) Supersonic flow: All variables are fixed with their freestream flow values.

(c) Exit condition:

(c.1) Subsonic flow: Four characteristic directions of information propagation point outward the computational domain and should be extrapolated from interior information ([33]). The characteristic direction associated to the "$(q_n\text{-}a)$" velocity should be specified because it penetrates the calculation domain. In this case, the ghost volume's pressure is specified by its freestream value. Density and velocity components are extrapolated and the total energy is obtained by the state equation of a perfect gas.

(c.2) Supersonic flow: All variables are extrapolated from the interior domain due to the fact that all five characteristic directions of information propagation of the Euler equations point outward the calculation domain and, with it, nothing can be fixed.

10 Results

Tests were performed in a personal computer (notebook) with Pentium dual core processor of 2.20GHz of clock and 2.0Gbytes of RAM memory. Converged results occurred to 3 orders of reduction in the value of the maximum residual. The maximum residual is defined as the maximum value obtained from the discretized conservation equations. The value used to γ was 1.4. To all problems, the attack or entrance angle was adopted equal to 0.0°.

The physical problems to be studied are the supersonic flows along a compression corner and along a ramp, to the inviscid case, and the transonic flow along a convergent-divergent nozzle, viscous case.

10.1 Ramp Physical Problem – Inviscid Case

The ramp configuration is described in Fig. 1. The ramp inclination angle is 20^o. An algebraic mesh of 61x60x10 points or composed of 31,860 hexahedrons and 36,600 nodes was used as shown in Fig. 2. The points are equally spaced in both directions.

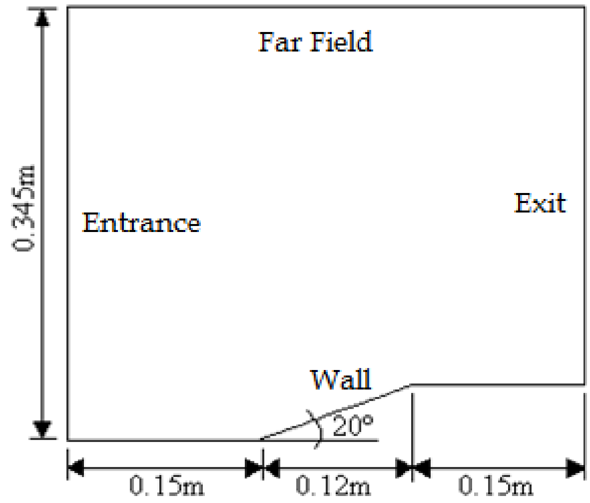

Figure 1. Ramp configuration.

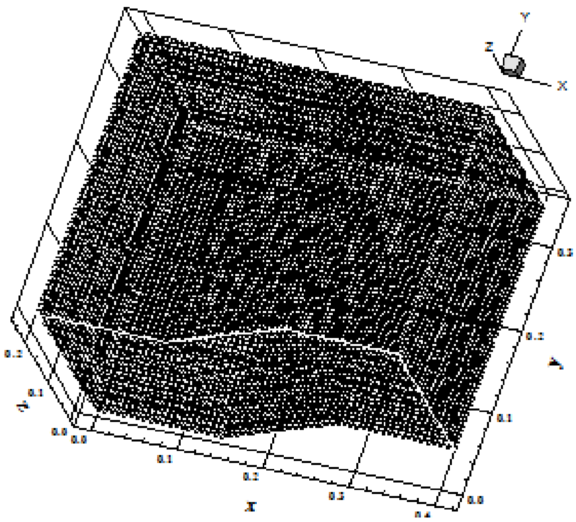

Figure 2. Ramp mesh (61x60x10).

This problem consists in a low supersonic flow impinging a ramp, where an oblique shock wave and an expansion fan are generated. The freestream Mach number is equal to 2.0. The solutions are compared with the oblique shock wave theory and the Prandtl-Meyer expansion fan theory.

10.1.1 Lax and Wendroff solutions

Figures 1 to 7 exhibits the pressure contours of the [7] scheme in its five versions, namely: Min1 (Minmod1), Min2 (Minmod2), Min3 (Minmod3), SB (Super Bee), and VL (Van Leer). The contours present good characteristics, without oscillations, and the most severe pressure field is due to the [7] scheme in its SB variant. The SB variant also captures the shock with the smallest width.

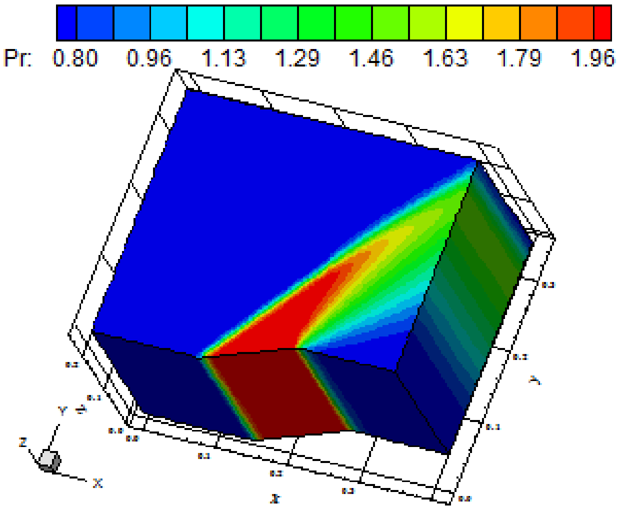

Figure 3. Pressure contours ([7]-Min1).

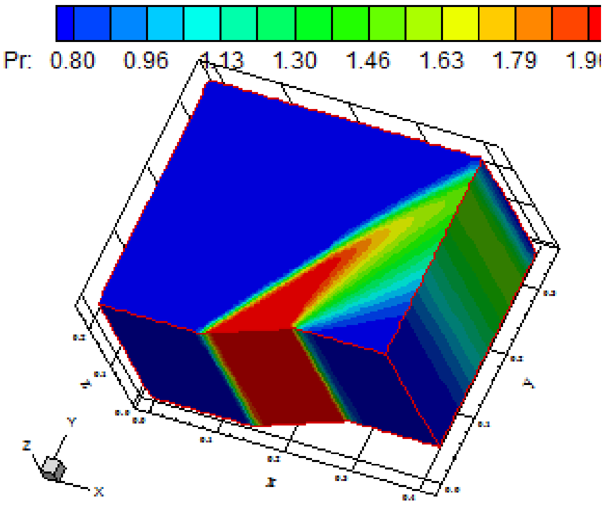

Figure 4. Pressure contours ([7]-Min2).

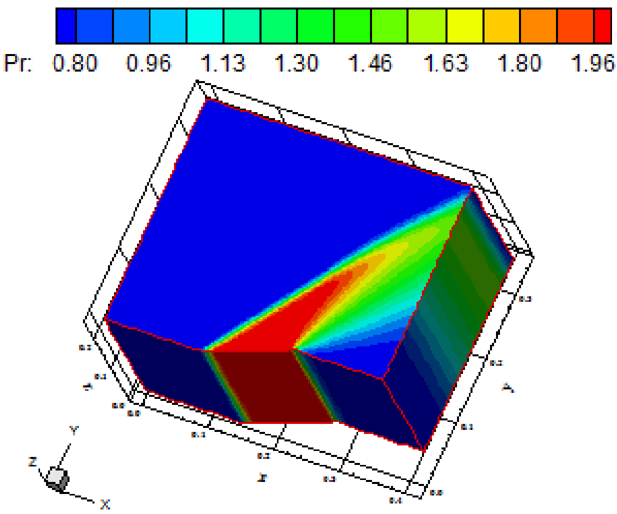

Figure 5. Pressure contours ([7]-Min3).

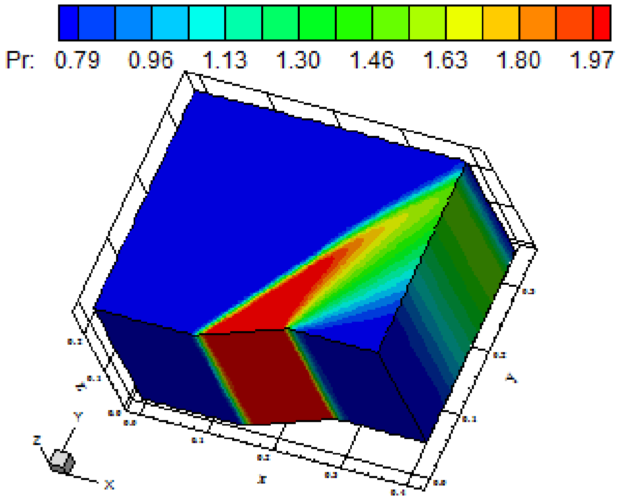

Figure 6. Pressure contours ([7]-SB).

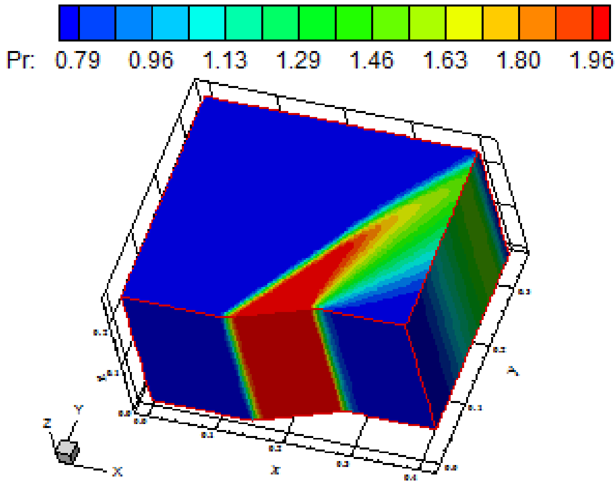

Figure 7. Pressure contours ([7]-VL).

Figure 8 presents the pressure distribution at wall, at k = KMAX/2, where KMAX is the maximum number of nodes in the k direction. These pressure distributions are compared with the oblique shock wave theory and the Prandtl-Meyer expansion wave theory results. As can be observed, the pressure plateau is well captured by the scheme in its five variants. A better behavior is observed at the expansion fan captured by the SB non-linear limiter. It detects the fan closer to the theory profile. All solutions capture the shock discontinuity with four cells, which is a reasonable solution to a high resolution scheme.

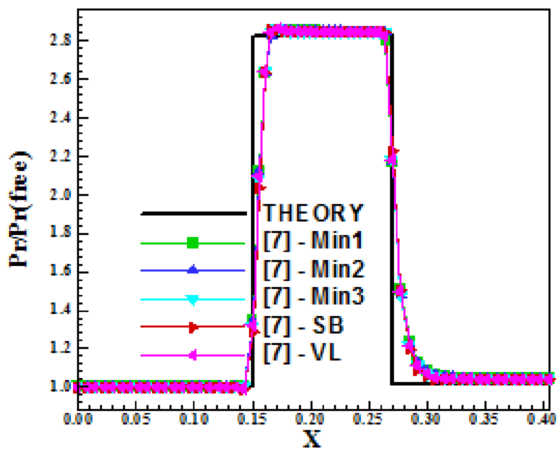

Figure 8. Wall pressure distribution.

10.1.2 Yee, Warming and Harten solutions

Figure 9 exhibits the pressure contours obtained by the [12] scheme. As can be observed, a pressure peak exists at the corner beginning which results in a severe pressure peak at the wall pressure distribution, damaging the solution quality of this scheme.

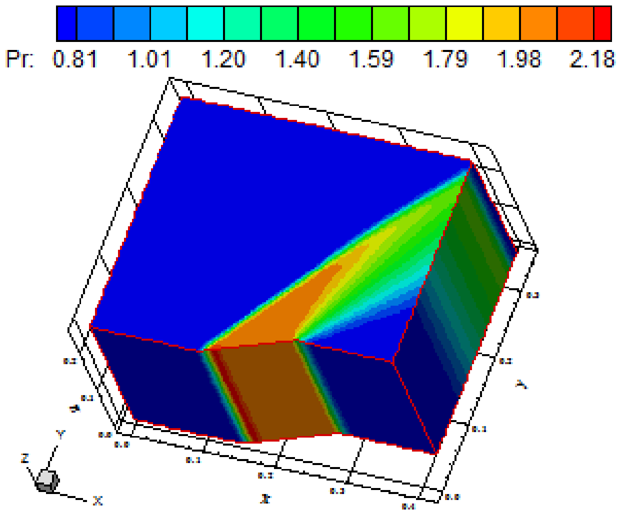

Figure 9. Pressure contours ([12]).

Other consequence is the value of the maximum field pressure, which is a numerical value, but not a physical value. This solution loses in quality in comparison with the other solutions.

Figure 10 presents the pressure distribution at wall in k = KMAX/2. As aforementioned, it exists a pressure peak at the shock discontinuity. It is very strength and prejudices the solution quality of this scheme. The shock discontinuity is captured using four cells, which is a reasonable result for a high resolution scheme.

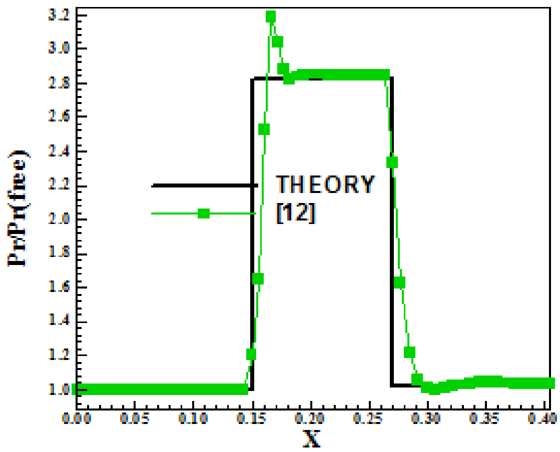

Figure 10. Wall pressure distribution.

10.1.3 Yee solutions

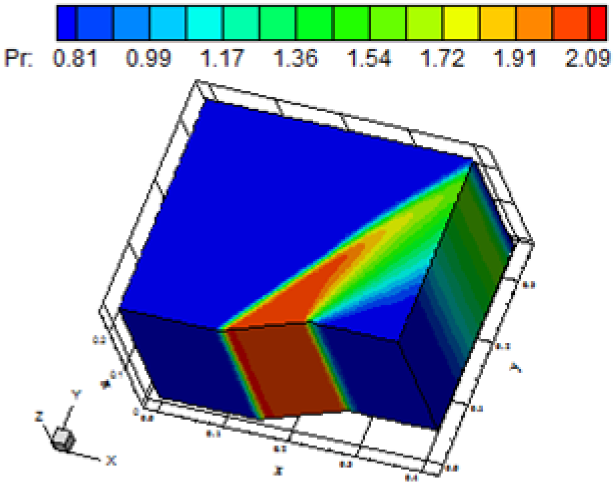

Figure 11. Pressure contours ([9]-Min1).

Figures 11 to 14 show the pressure contours to the [9] scheme in its four variants: Min1, Min2, Min3, and VL. The SB variant did not present converged results. Figure 11 presents a discrete pressure peak at the corner beginning. Observing all other solutions, it is also possible to note that all of them present pressure oscillations at the corner. The worse result is in Fig. 13, with Min3 variant.

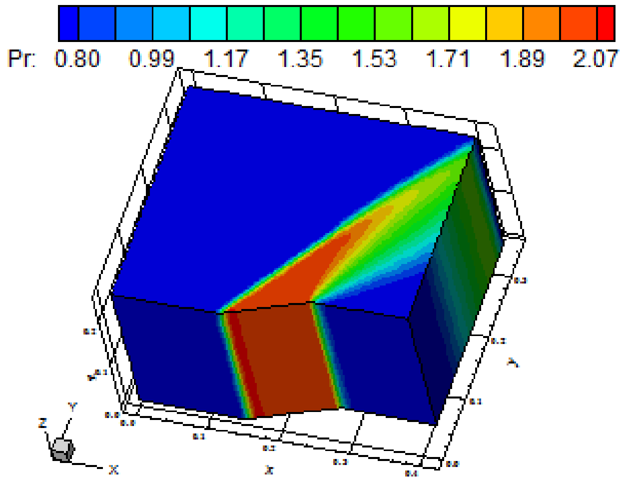

Figure 12. Pressure contours ([9]-Min2).

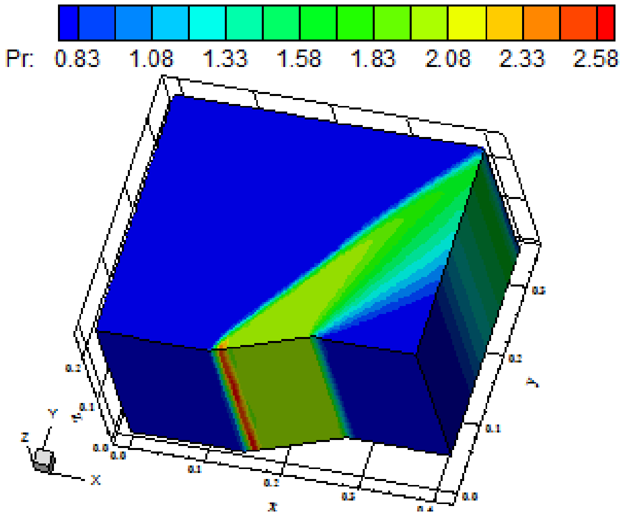

Figure 13. Pressure contours ([9]-Min3).

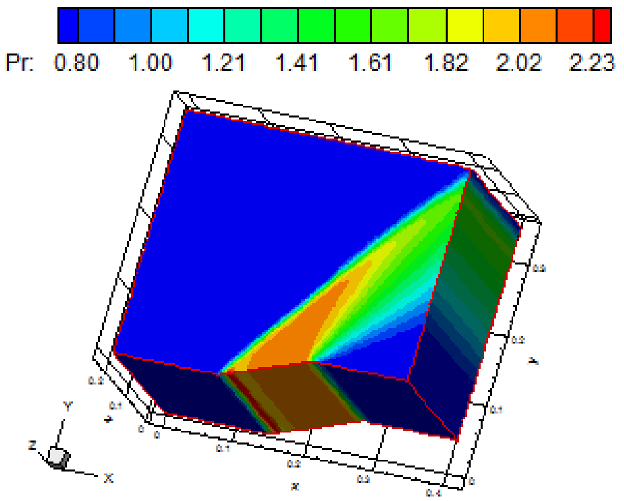

Figure 14. Pressure contours ([9]-VL).

Figure 15 shows the wall pressure distribution obtained by the four variants of the [9] scheme. The solution with the variant Min2 is that present the smallest peak, even so very strength than the [7] solutions. Moreover, the shock wave discontinuity is captured using four cells.

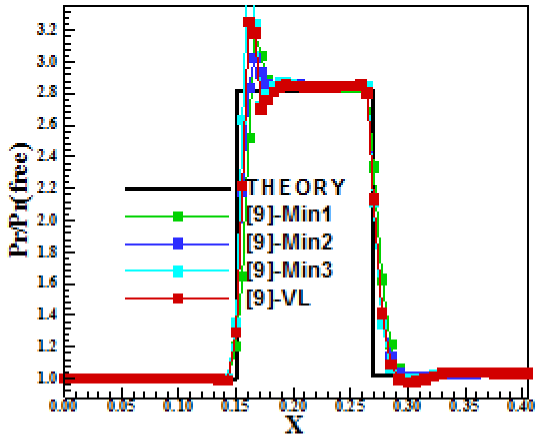

Figure 15. Wall pressure distributions.

10.1.4 Harten and Osher solutions

Figures 16 and 17 exhibit the pressure contours obtained by the [13] scheme, in its two versions. There are not pressure oscillations and these ones are clear and sharp defined. Good homogeneity properties are observed at the k planes.

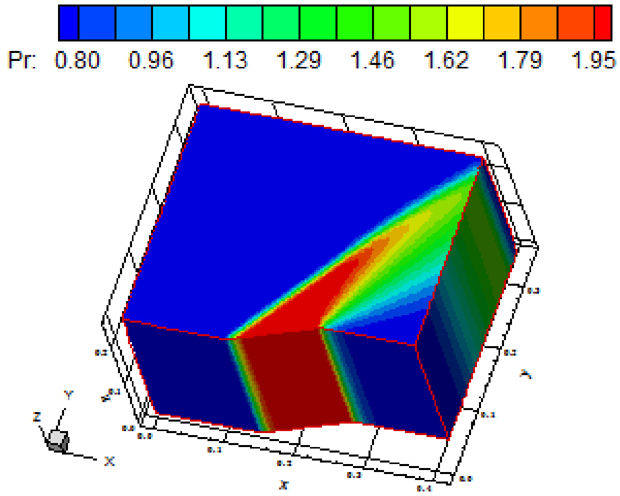

Figure 16. Pressure contours ([13]-TVD).

Figure 18 exhibits the wall pressure distributions of the [13] scheme in its two versions, namely: TVD and ENO. As can be observed, these solutions are the best, with a little improvement to the ENO solution at the fan region. The shock is captured using four cells and the shock plateau is far smooth, conducting to smoothest solutions.

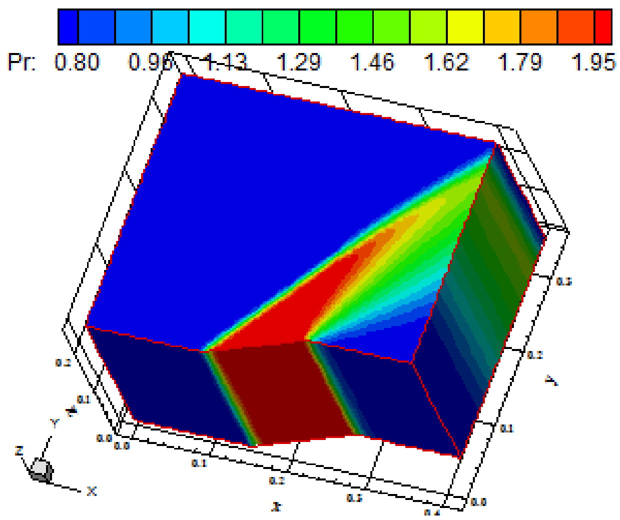

Figure 17, Pressure contours ([13]-ENO),

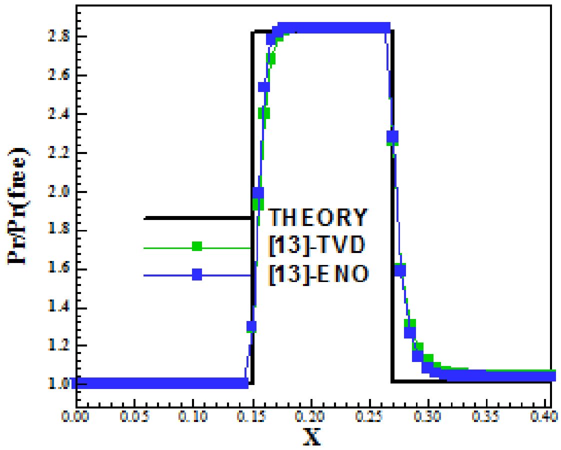

Figure 18. Wall pressure distributions,

A way to quantitatively verify if the solutions generated by each scheme are satisfactory consists in determining the shock angle of the oblique shock wave, β, measured in relation to the initial direction of the flow field. [42] (pages 352 and 353) presents a diagram with values of the shock angle, β, to oblique shock waves. The value of this angle is determined as function of the freestream Mach number and of the deflection angle of the flow after the shock wave, ϕ. To ϕ = 20º (ramp inclination angle) and to a freestream Mach number equals to 2.0, it is possible to obtain from this diagram a value to β equals to 53.0 º. Using a transfer in all pressure contours figures, it is possible to obtain the values of β to each scheme, as well the respective errors, shown in Tab. 1. As can be noted, the best results are due to [12], [9] – Min2, and [13] – ENO. As the best wall pressure distribution was due to [13] – ENO and the best shock angle also have the [13] – ENO algorithm as one of the best schemes solutions, the [13] – ENO algorithm is the best in this ramp problem.

Table 1. Shock angle and percentage errors.

Algorithm	B (º)	Error (%)
[7] – Min1	53.2	0.38
[7] – Min2	53.2	0.38
[7] – Min3	53.4	0.75
[7] – SB	53.2	0.38
[7] – VL	53.5	0.94
[12]	53.0	0.00
[9] – Min1	53.1	0.19
[9] – Min2	53.0	0.00
[9] – Min3	53.1	0.19
[9] – VL	54.0	1.89
[13] – TVD	53.2	0.38
[13] – ENO	53.0	0.00

10.2 Compression Corner Physical Problem – Inviscid Case

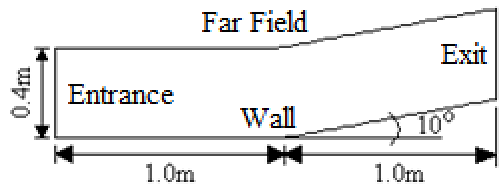

Figure 19. Compression corner configuration.

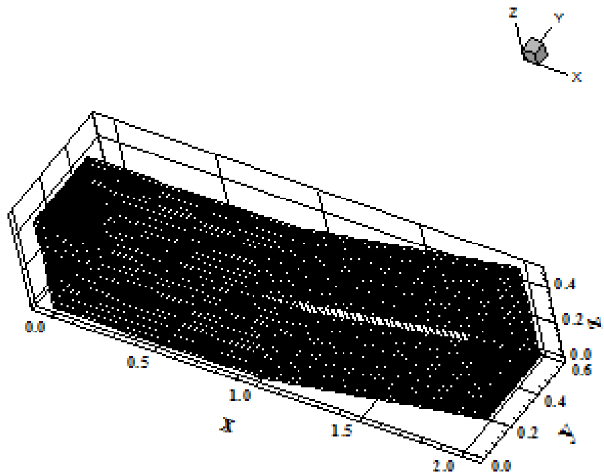

Figure 20. Compression corner mesh (70x50x10).

The compression corner configuration is described in Fig. 19. The corner inclination angle is 10º. An algebraic mesh of 70x50x10 points or composed of 30,429 hexahedral cells and 35,000 nodes was used and is shown in Fig. 20. The points are equally spaced in both directions.

10.2.1 Lax and Wendroff solutions

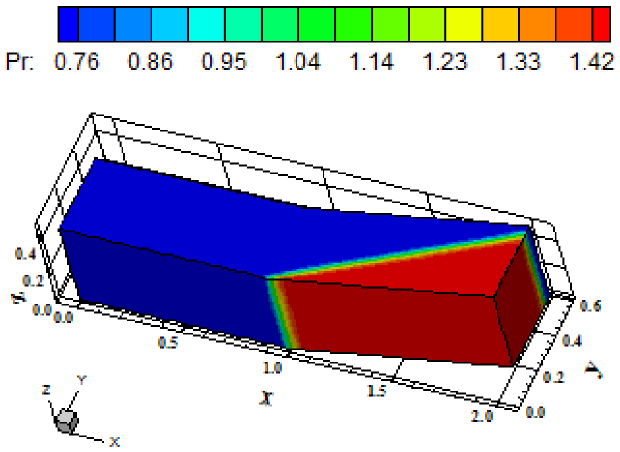

Figure 21. Pressure contours ([7]-Min1).

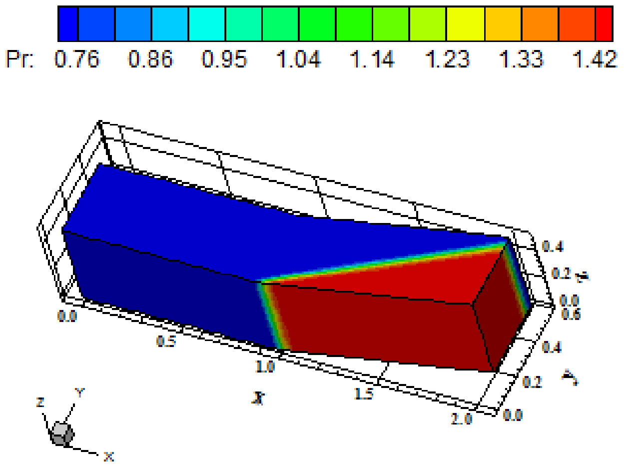

Figure 22. Pressure contours ([7]-Min2).

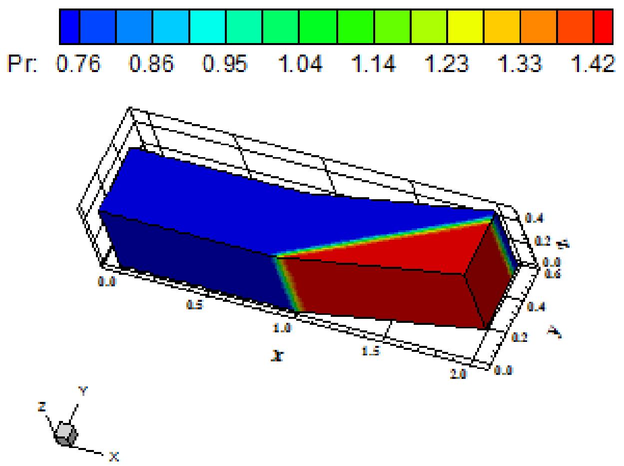

Figure 23. Pressure contours ([7]-Min3).

This problem consists in a moderate supersonic flow impinging a compression corner, where an oblique shock wave is generated. The freestream Mach number is equal to 3.0. The solutions are compared with the oblique shock wave theory results.

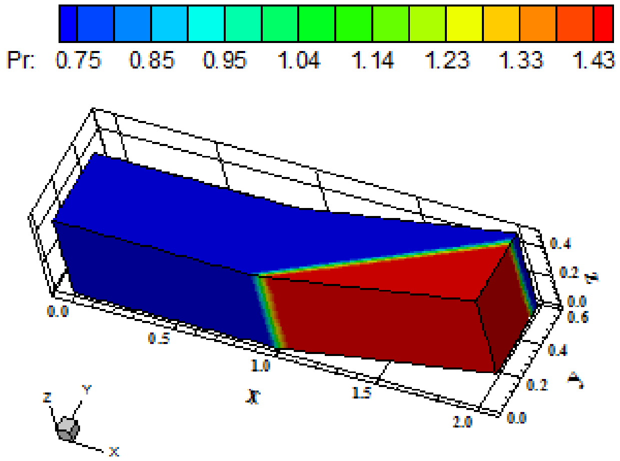

Figure 24. Pressure contours ([7]-SB).

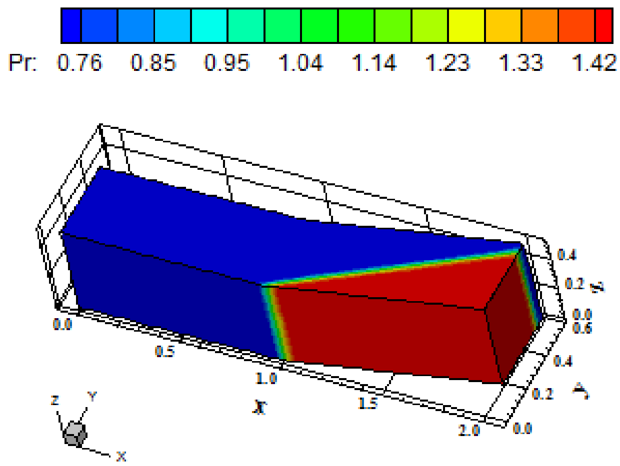

Figure 25. Pressure contours ([7]-VL).

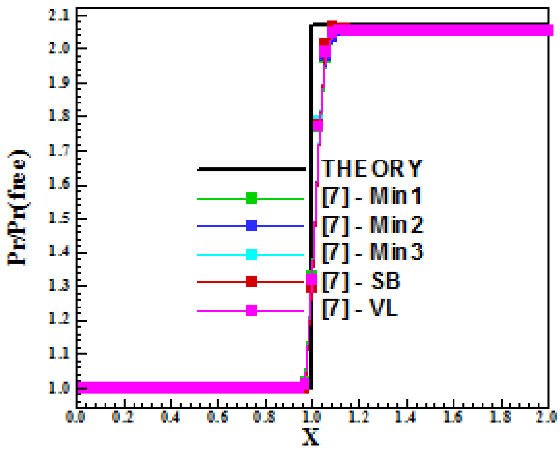

Figure 26. Wall pressure distributions ([7]).

Figures 21 to 25 exhibit the pressure contours obtained by the [7] scheme, in its five variants. The most intense pressure field is due to the “Super Bee” solution. All solutions are of good quality, without pressure oscillations. The “Gibbs” phenomenon is not perceived in the “Super Bee” solution.

Figure 26 presents the wall pressure distributions obtained by [7], in its five variants, along the compression corner. They are compared with the oblique shock wave theory results. The reference solution is due to the Van Leer limiter. All variants capture the shock wave using four cells.

10.2.2 Yee, Warming and Harten solutions

Figure 27 presents the pressure contours obtained by the [12] algorithm. A pressure peak is observed at the corner beginning and is apparent in the wall pressure distributions (Fig. 28). It damages the solution quality of this scheme.

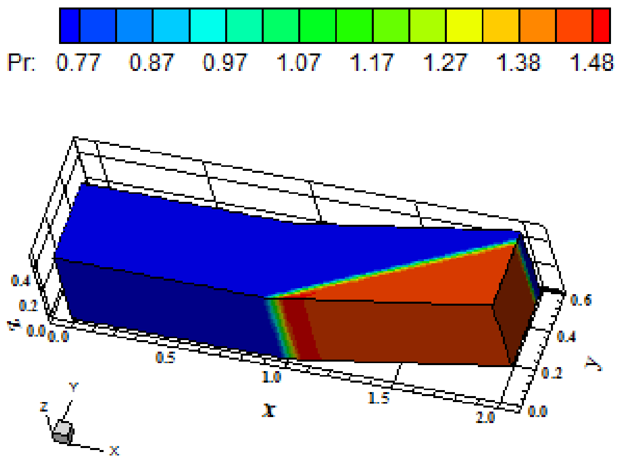

Figure 27. Pressure contours ([12]).

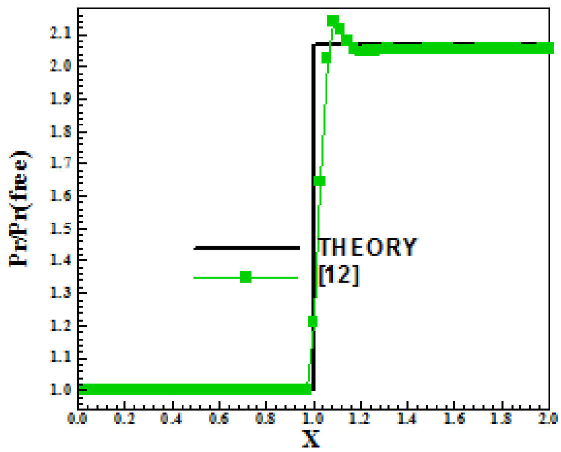

Figure 28. Wall pressure distribution ([12]).

As can be seen from Fig. 28, the wall pressure distribution presents a oscillation at the corner, which damages its quality. The shock profile is captured in four cells.

10.2.3 Yee solutions

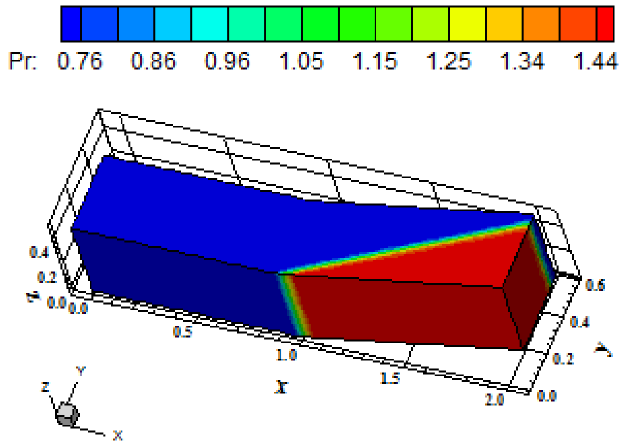

Figure 29. Pressure contours ([9]-Min1).

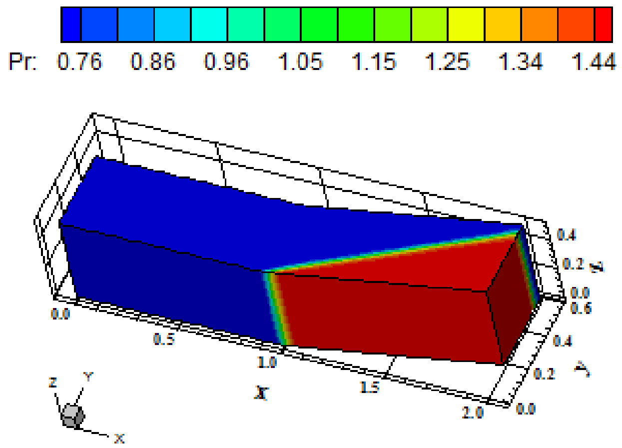

Figure 30. Pressure contours ([9]-Min2).

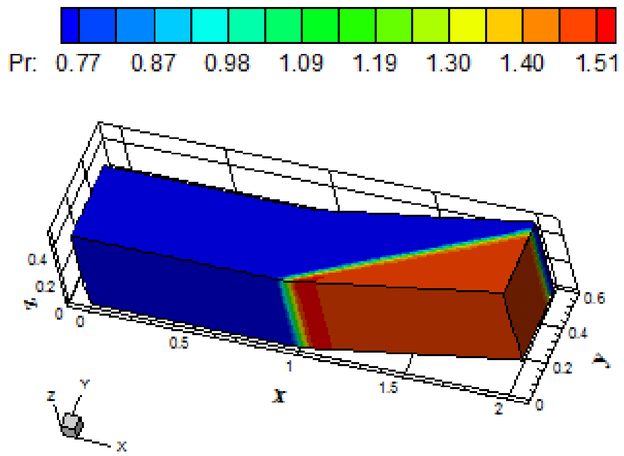

Figure 31. Pressure contours ([9]-Min3).

Figures 29 to 33 show the pressure contours obtained by the [9] algorithm in its five variants. As can be observed, with the exception of the solutions generated by Min1 and Min2, all others present pressure peak at the corner beginning. The solution generated by the "Super Bee" limiter is the worse.

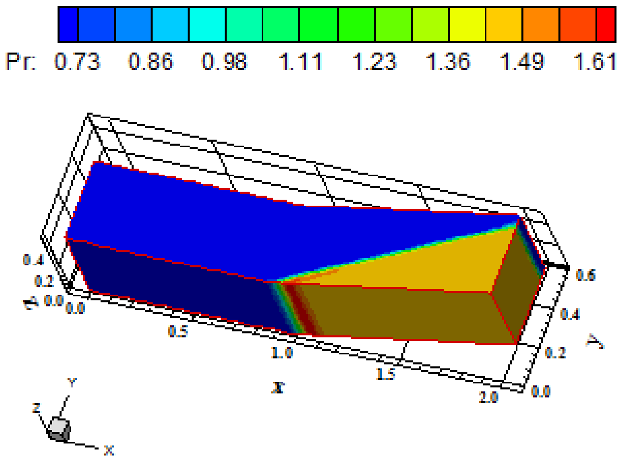

Figure 32. Pressure contours ([9]-SB).

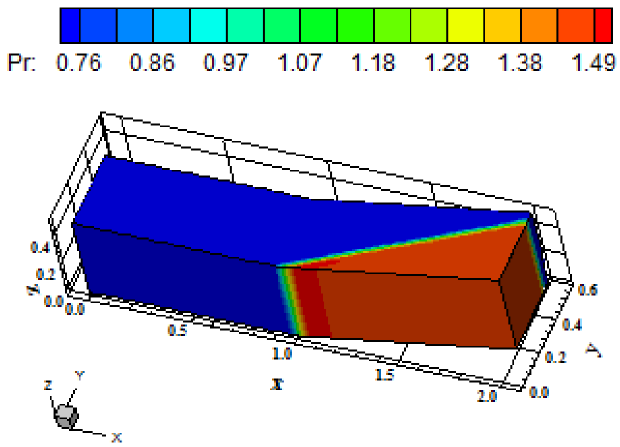

Figure 33. Pressure contours ([9]-VL).

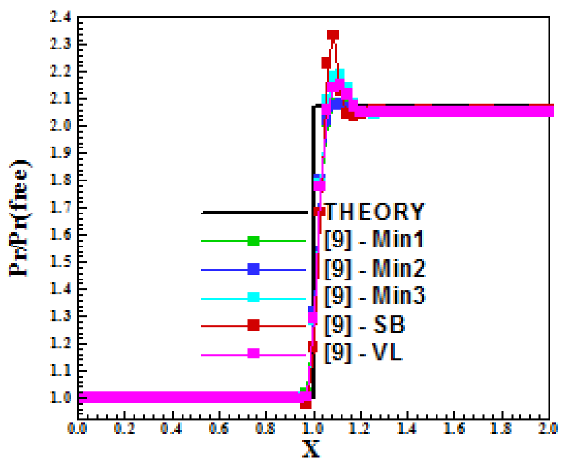

Figure 34. Wall pressure distributions ([9]).

Figure 34 shows the wall pressure distributions obtained by the [9] scheme in its five variants. The reference solution is that due to the Min2 limiter, presenting a small peak in comparison with the other solutions. The shock is captured using five cells, which is bad for a high resolution scheme.

10.2.4 Harten and Osher solutions

Finally, Figures 35 and 36 exhibit the pressure contours to the solutions obtained by the TVD and ENO schemes of [13], respectively. Both solutions are of good quality, without pressures peaks or oscillations.

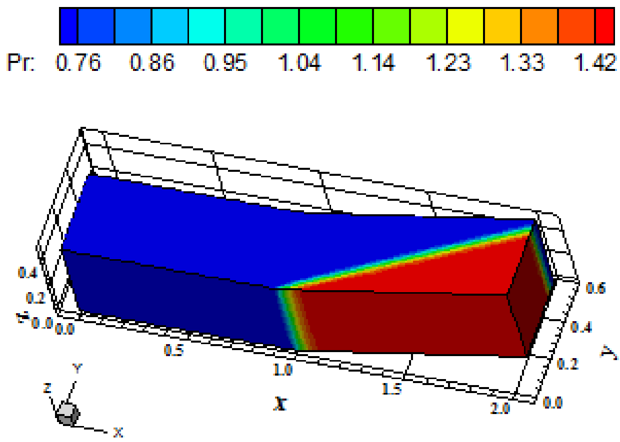

Figure 35. Pressure contours ([13]-TVD).

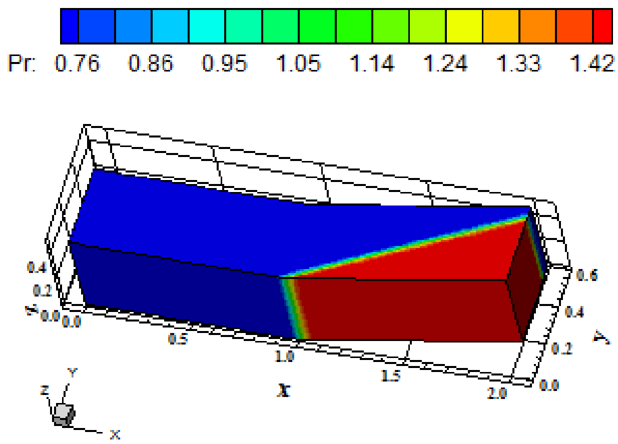

Figure 36. Pressure contours ([13]-ENO).

Figure 37 shows the wall pressure distributions resulting from [13] scheme. The solution obtained by the ENO procedure is the reference one to the [13] scheme. The shock is captured in four cells.

Comparing all wall pressure distributions, the best solution is due to [13] in its ENO version.

As said in the ramp problem, one way to quantitatively verify if the solutions generated by each scheme are satisfactory consists in determining the shock angle of the oblique shock wave, β, measured in relation to the initial direction of the flow field.

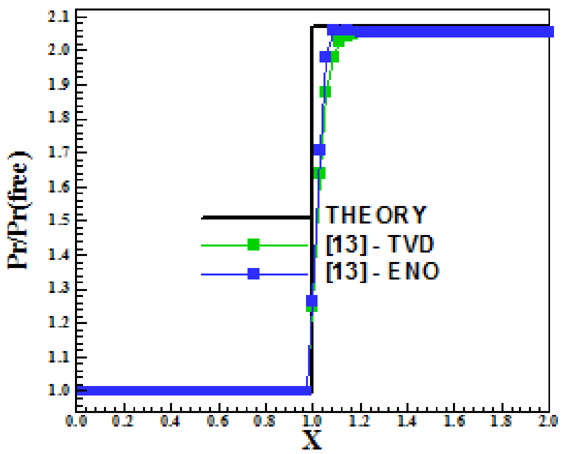

Figure 37. Wall pressure distributions ([13]).

To the compression corner problem, ϕ = 10º (ramp inclination angle) and the freestream Mach number is 3.0, resulting from the [42] diagram a value to β equals to 27.5º. Using a transfer in the pressure fields in the xy plane, it is possible to obtain the values of β to each scheme, as well the respective errors, shown in Tab. 2. As can be observed, the [9] TVD scheme, in its Min3 version, has yielded the best result. Errors less than 2.20% were observed in all solutions.

Table 2. Shock angle and percentage errors.

Algotithm	β (°)	Error (%)
[7] – Min1	27.4	0.36
[7] – Min2	27.3	0.73
[7] – Min3	27.1	1.45
[7] – SB	28.0	1.82
[7] – VL	27.4	0.36
[12]	26.9	2.18
[9] – Min1	27.0	1.82
[9] – Min2	27.7	0.73
[9] – Min3	27.5	0.00
[9] – SB	27.4	0.36
[9] – VL	27.0	1.82
[13] - TVD	27.0	1.82
[13] - ENO	27.1	1.45

10.3 Convergent-Divergent Nozzle - Viscous

To the viscous case, it was chosen the convergent-divergent nozzle problem. The computational domain and the mesh configuration are described in Figs. 38 and 39, respectively. The mesh is composed of 42,000 hexahedron cells and 43,310 nodes on a finite volume context (equivalent to a mesh of 61x71x10 points in finite differences). Only the [7] algorithm, in its Min1 and Min2 variants, yielded converged results.

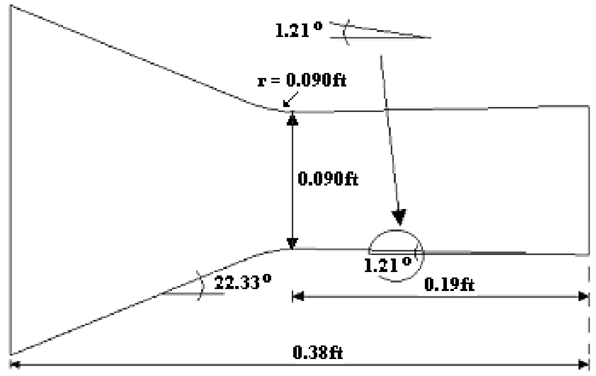

Figure 38. Nozzle configuration.

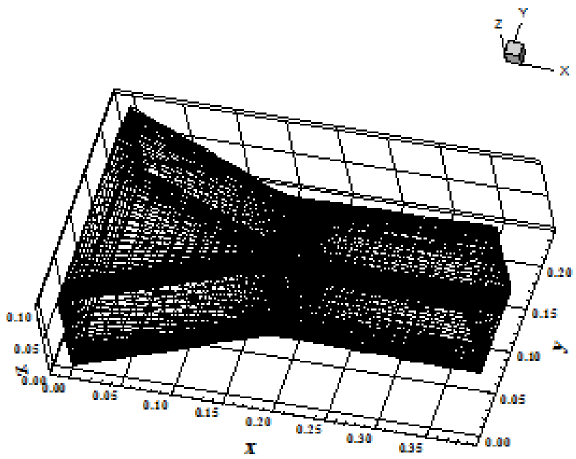

Figure 39. Mesh configuration.

The initial condition to this problem considers a stagnation flow. The Reynolds number was estimated in $1.32x10^5$, according to [32], considering the characteristic length of 0.027m and an altitude of 0.0m.

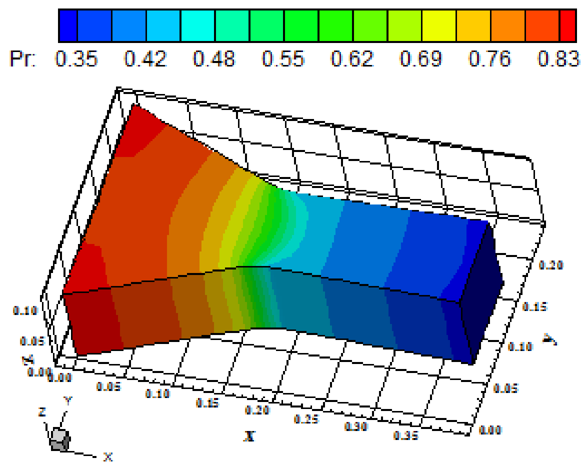

Figure 40. Pressure contours ([7]–Min1).

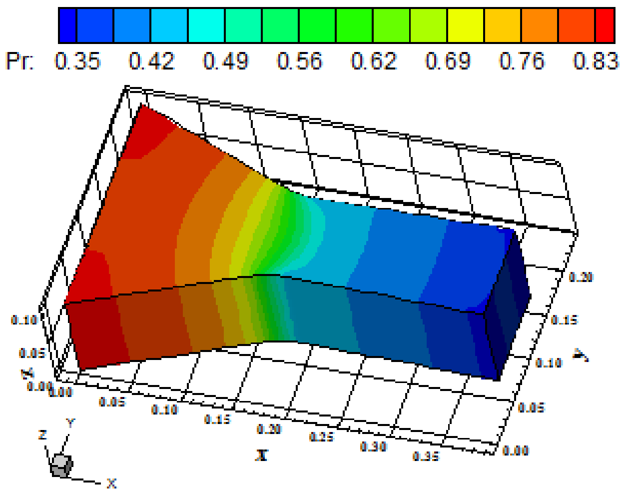

Figure 41. Pressure contours ([7]-Min2).

Figures 40 and 41 exhibit the pressure contours obtained by the [7] scheme, in its Min1 and Min2 variants, respectively. The most severe pressure field is due to the Min2 version of the [7] algorithm.

Figure 42 shows the wall pressure distribution obtained by the [7] in its two variants. They are compared with the experimental results of [42]. As can be observed, the reasonable solution is obtained by the [7] scheme using Min1 limiter. Hence, it is possible to conclude that for the laminar viscous results, the [7] scheme, in its Min1 version, provides the best solution.

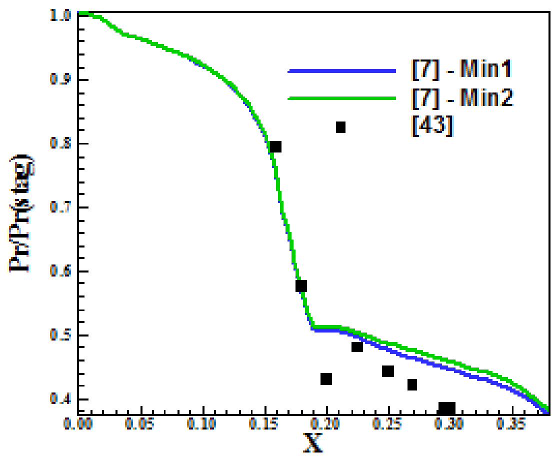

Figure 42. Wall pressure distribution ([7]).

11 Conclusion

In the present work, the [7] TVD symmetric, the [9] TVD symmetric, the [12] TVD, and the [13] TVD/ENO schemes are implemented, on a finite volume context and using a structured spatial discretization, to solve the Euler and Navier-Stokes equations in the three-dimensional space. With the exception of [7; 9], all others schemes are high resolution flux difference splitting ones, based on the concept of Harten's modified flux function. The [7; 9] TVD schemes are symmetric ones, incorporating TVD properties due to the appropriated definition of a limited dissipation function. All schemes are second order accurate in space. An implicit formulation is employed to solve the Euler equations, whereas a time splitting method, an explicit method, is used to solve the Navier-Stokes equations. An approximate factorization in Linearized Nonconservative Implicit LNI form is employed by the [12-13] schemes, whereas an approximate factorization ADI method is employed by the [7; 9] schemes. All algorithms are first order accurate in time. The algorithms are accelerated to the steady state solution using a spatially variable time step, which has demonstrated effective gains in terms of convergence rate ([30-31]). All schemes are applied to the solution of physical problems of the supersonic flows along a ramp and along a compression corner, in the inviscid case, whereas in the laminar viscous case, the supersonic flow along a convergent-divergent nozzle is solved.

The results have demonstrated that the [9] algorithm, with Min2 non-limiter, and [13], in its ENO version, has presented the best solutions in the inviscid ramp and compression corner problems; In the viscous problem, the [7] algorithm, in its Min1 variant, has presented the best solution in the viscous nozzle problem.

This work is the first part of this study, which compares different TVD and ENO algorithms. The next paper will treat more four numerical algorithms based on the Yee's and Yang's works.

12 Acknowledgments

The author acknowledges the CNPq by the financial support conceded under the form of a DTI (Industrial Technological Development) scholarship no. 384681/2011-5. He also acknowledges the infra-structure of the ITA that allowed the realization of this work.

References:

[1] R. D. Richtmeyer, and K. W. Morton, *Difference Methods for Initial-Value Problem*, Interscience-Wiley, New York, 1967.

[2] A. Harten, On a Class of High Resolution Total Variation-Stable Finite Difference Schemes, *NYU Report*, New York University, New York, October, 1982.

[3] A. Harten, High Resolution Schemes for Hyperbolic Conservation Laws, *Journal of Computational Physics*, Vol. 49, No. 2, 1983, pp. 357-393.

[4] A. Harten, J. M. Hyman, and P. D. Lax, *Commun. Pure Appl. Math*, Vol. 29, 1976, p. 297.

[5] M. G. Crandall, and A. Majda, *Math. Comput.*, Vol. 34, No. 149, 1980, p. 1.

[6] P. L. Roe, Generalized Formulation of TVD Lax-Wendroff Schemes, *ICASE Report No. 84-53*, 1984.

[7] P. D. Lax, and B. Wendroff, Difference Schemes for Hyperbolic Equations with High Order of Accuracy, *Communications on Pure and Applied Mathematics*, Vol. XVII, 1964, pp. 381-398.

[8] S. F. Davis, TVD Finite Difference Schemes and Artificial Viscosity, *ICASE Report No. 84-20*, 1984.

[9] H. C. Yee, Construction of Explicit and Implicit Symmetric TVD Schemes and Their Applications, *Journal of Computational Physics*, Vol. 68, 1987, pp. 151-179.

[10] A. Harten, On a Class of High Resolution Total-Variation-Stable Finite-Difference Schemes", *SIAM Journal Numerical Analysis*, Vol. 21, 1984, p. 1.

[11] H. C. Yee, R. F. Warming, and A. Harten, In Proceedings of the AMS-SIAM Summer Seminar on Large-Scale Computation in Fluid Mechanics, edited by B. E. Engquist *et al.*, *Lectures in Applied Mathematics*, Vol. 22, 1983, p. 357.

[12] H. C. Yee, R. F. Warming, and A. Harten, Implicit Total Variation Diminishing (TVD) Schemes for Steady-State Calculations, *Journal of Computational Physics*, Vol. 57, No. 3, 1985, pp. 327-360.

[13] A. Harten, and S. Osher, Uniformly High Order Accurate Non-Oscillatory Schemes, *SIAM J. Num. Anal.*, Vol. 24, No. 2, 1987, pp. 279-309.

[14] A. Harten, B. Engquist, S. Osher, and S. R. Chakravarthy, Uniformly High Order Accurate Essentially Non-Oscillatory Schemes. II., *Preprint*, 1986.

[15] A. Harten, B. Engquist, S. Osher, and S. R. Chakravarthy, Some Results on Uniformly High Order Accurate Essentially Non-Oscillatory Schemes, *Advances in Numerical Analysis and Applied Mathematics*, edited by J. C. South, Jr. and M. Y. Hussaini, *ICASE Rept. 86-18*; also *Journal of Applied Num. Mathematics* Vol. 2, 1986, pp. 347-367.

[16] A. Harten, B. Engquist, S. Osher, and S. R. Chakravarthy, Uniformly High Order Accurate Essentially Non-Oscillatory Schemes. III., *ICASE Rept. 86-22*, 1986.

[17] S. K. Godunov, A Finite Difference Method for the Numerical Computation of Discontinuous Solutions of the Equations to Fluid Dynamics, *Mat. Sb*., Vol. 47, 1958, pp. 271-290.

[18] B. Van Leer, Towards the Ultimate Conservative Difference Scheme. V. A Second Order Sequel to Godunov's Method, *Journal of Computational Physics*, Vol. 32, No. 1, 1979, pp. 101-136.

[19] P. Colella, and P. R. Woodward, The Piecewise-Parabolic Method (PPM) for Gas-Dynamical Simulations, *Journal of Computational Physics*, Vol. 54, No. 1, 1984, pp. 174-201.

[20] S. Osher, and S. R. Chakravarthy, High Resolution Schemes and Entropy Conditions, *SIAM Journal of Numerical Analysis*, Vol. 21, No. 4, 1984, pp. 955-984.

[21] A. Harten, Preliminary Results on the Extension of ENO Schemes to Two-Dimensional Problems, *Proceedings of the International Conference on Hyperbolic Problems*, Saint-Etienne, France, 1986.

[22] H. C. Yee, A Class of High Resolution Explicit and Implicit Shock-Capturing Methods, *NASA TM-101088*, 1989.

[23] P. L. Roe, Characteristic-based Schemes for the Euler Equations, *Annual Review of Fluid Mechanics*, Vol. 18, 1986, pp. 337-365.

[24] G. Moretti, Computation of Flows with Shocks, *Annual Review of Fluid Mechanics*, Vol. 19, 1987, pp. 313-337.

[25] R. M. Beam, and R. F. Warming, An Implicit Factored Scheme for the Compressible Navier-Stokes Equations, *AIAA Journal*, Vol. 16, No. 4, 1978, pp. 393-402.

[26] J. Douglas, On the Numerical Integration of $u_{xx}+u_{yy}=u_t$ by Implicit Methods", Journal of the Society of Industrial and Applied Mathematics, Vol. 3, 1955, pp. 42-65.

[27] D. W. Peaceman, and H. H. Rachford, The Numerical Solution of Parabolic and Elliptic Differential Equations, *Journal of the Society of Industrial and Applied Mathematics*, Vol. 3, 1955, pp. 28-41.

[28] J. Douglas, and J. E. Gunn, A General Formulation of Alternating Direction Methods, Numerische Mathematiks, Vol. 6, 1964, pp. 428-453.

[29] N. N. Yanenko, *The Method of Fractional Steps*, Springer Verlag, N.Y., EUA, 1971.

[30] E. S. G. Maciel, Analysis of Convergence Acceleration Techniques Used in Unstructured Algorithms in the Solution of Aeronautical Problems – Part I, *Proceedings of the XVIII International Congress of Mechanical Engineering (XVIII COBEM)*, Ouro Preto, MG, Brazil, 2005. [CD-ROM]

[31] E. S. G. Maciel, Analysis of Convergence Acceleration Techniques Used in Unstructured Algorithms in the Solution of Aerospace Problems – Part II, *Proceedings of the XII Brazilian Congress of Thermal Engineering and Sciences (XII ENCIT)*, Belo Horizonte, MG, Brazil., 2008 [CD-ROM]

[32] R. W. Fox, and A. T. McDonald, *Introdução à Mecânica dos Fluidos*, Ed. Guanabara Koogan, Rio de Janeiro, RJ, Brazil, 632p, 1988.

[33] E. S. G. Maciel, Simulação Numérica de Escoamentos Supersônicos e Hipersônicos Utilizando Técnicas de Dinâmica dos Fluidos Computacional, *Doctoral Thesis*, ITA, CTA, São José dos Campos, SP, Brazil, 258p, 2002.

[34] E. S. G. Maciel, Relatório ao Conselho Nacional de Pesquisa e Desenvolvimento Tecnológico (CNPq) sobre as Atividades de Pesquisa Desenvolvidas no Terceiro Ano de Vigência da Bolsa de Estudos para Nível DCR-IF Referente ao Processo No. 304318/2003-5, *Report to the National Council of Scientific and Technological Development (CNPq)*, Recife, PE, Brazil, 52p, 2006. [available in the website www.edissonsavio.eng.br]

[35] P. L. Roe, Approximate Riemann Solvers, Parameter Vectors, and Difference Schemes, *Journal of Computational Physics*, Vol. 43, No. 2, 1981, pp. 357-372.

[36] E. S. G. Maciel, Explicit and Implicit TVD and ENO High Resolution Algorithms Applied to the Euler and Navier-Stokes Equations in Three-Dimensions – Theory, *Proceedings of the 20th International Congress of Mechanical Engineering (XX COBEM)*, Gramado, RS, Brazil. [CD-ROM]

[37] P. L. Roe, In Proceedings of the AMS-SIAM Summer Seminar on Large-Scale Computation in Fluid Mechanics, edited by B. E. Engquist *et al.*, *Lectures in Applied Mathematics*, (Amer. Math. Soc., Providence, R. I., 1985), Vol. 22, 1983, p. 163.

[38] B. Van Leer, Towards the Ultimate Conservative Difference Scheme. II. Monotonicity and Conservation Combined in a Second-Order Scheme, *Journal of Computational Physics*, Vol. 14, 1974, pp. 361-370.

[39] H. C. Yee, R. F. Warming, and A. Harten, A High-Resolution Numerical Technique for Inviscid Gas-Dynamic Problems with Weak Solutions, *Proceedings of the 8th International Conference on Numerical Methods in Fluid Dynamics*, E. Krause, Editor, Lecture Notes in Physics, Springer-Verlag, Berlim, Germany, Vol. 170, 1982, pp. 546-552.

[40] A. Jameson, and D. Mavriplis, Finite Volume Solution of the Two-Dimensional Euler Equations on a Regular Triangular Mesh, *AIAA Journal*, Vol. 24, 1986, pp. 611-618.

[41] J. T. Batina, Implicit Upwind Solution Algorithms for Three-Dimensional Unstructured Meshes, *AIAA Journal*, Vol. 31, No. 5, 1993, pp. 801-805.

[42] J. D. Anderson Jr., *Fundamentals of Aerodynamics*, McGraw-Hill, Inc., EUA, 563p, 1984.

[43] M. L. Mason, L. E. Putnam, and R. J. Re, The Effect of Throat Contouring on Two-Dimensional Converging-Diverging Nozzles at Sonic Conditions, *NASA Technical Paper 1704*, 1980.